Insights about the Ability of Folate based Supramolecular Gels to Act as Targeted Therapeutic Agents

Carla Rizzo[a‡] *Patrizia Cancemi,*[b‡] *Miriam Buttacavoli,*[b] *Gianluca Di Cara,*[b] *Cesare D'Amico,*[b] *Floriana Billeci,*[a,c] *Salvatore Marullo,*[a] *Francesca D'Anna*[a*]

[a]*Università degli Studi di Palermo, Dipartimento STEBICEF, Sezione di Chimica, Viale delle Scienze Ed. 17, 90128 Palermo (Italy)*

[b]*Università degli Studi di Palermo, Dipartimento STEBICEF, Sezione di Biologia Cellulare, Viale delle Scienze Ed. 16, 90128 Palermo (Italy)*

[c]*Until March 2022*

‡These authors contributed equally

*Corresponding author: Prof. F. D'Anna. E-mail: francesca.danna@unipa.it

Keywords: folate organic salts, self-assembly, supramolecular gels, antiproliferative activity, targeted therapeutic agents.

Abstract

With the aim to obtain targeted chemotherapeutic agents, imidazolium and ammonium-based folate salts were synthesized. Their photophysical behavior was investigated both in buffer and buffer/DMSO solution as well as in solid phase, performing UV-vis and fluorescence investigations. Properties of the aggregates were also analyzed by dynamic light scattering.

Gelation ability of the salts was analyzed in biocompatible solvents, and gel phases obtained were characterized by determining critical gelation concentrations and gel-solution transition temperatures. Insights about gelator interactions in the tridimensional network were also gained performing ATR-FTIR investigation. Properties of soft materials were further analyzed performing rheology measurements, scanning electron microscopy, fluorescence and resonance light scattering investigations.

Antiproliferative activity of organic salts was tested towards two breast cancer cell lines, expressing different levels of folate receptor, namely MDA-MB-231 and MCF-7, and a normal epithelial cell line, like h-TER T-RPE-1, by using MTT assay. Dichlodihydrofluorescein acetate test was performed to verify the role of oxidative stress in cell death. Finally, antiproliferative activity was also evaluated in gel phase, to verify if salts were able to retain biological activity also after the entrapment in the gelatinous network.

Results collected evidence that folate based organic salts were able to behave as targeted chemotherapeutic agents both in solution and gel phase, showing uptake mechanism and selectivity indexes that depend on both cancer cell line nature and salt structure.

Introduction

Cancer is currently one of the main causes of mortality worldwide[1] and war against different forms of this disease has brought about the obtainment of many chemotherapeutic agents. Unfortunately, traditional chemotherapeutic agents utilized in the treatment of cancer, have toxic effects, not only on tumor cells but also on the normal replicating cells, and obligating patients to discontinuous treatments. For these reasons, there is an urgent need for more selective chemotherapeutic agents and drug delivery methods to improve antitumor activity and side effect profiles.[2]

A useful strategy to pursue the above aim is represented by the targeted delivery. In this case, the chemotherapeutic drug is tethered to a specific ligand of a disease marker, via a releasable linker, inducing the drug accumulation at the desired site of action and increasing the dose efficiency with reducing side effects.[3,4] As for targeting ligands, antibodies, peptides and small proteins have been used, together with small molecules.[5-7] Among these latter, the use of folic acid has received considerable attention to deliver the attached drugs specifically to folate receptor-expressing cancer cells.[8,9]

Folic acid is a vitamin essential for the synthesis, repair, and methylation of DNA, as well as the

metabolism of amino acids and RNA. Generally, folate conjugate and folate-linked drugs do not show affinity for most normal cells, as the uptake of folate is mediated by either the reduced folate carrier[10] or the proton coupled folate transporter,[11] having no affinity for the above classes of compounds. However, folic acid can be also internalized through folate receptor, overexpressed on few cell types. In particular, the alpha isoform of folate receptor (FRα) is expressed on the apical surfaces of several epithelial cells, where it is inaccessible to parenterally administered folate species,[12] but it is also overexpressed on 40% of human cancers, where it is completely accessible to folate species.[13] Differently, the beta isoform of folate receptor is expressed on the surface of malignant cells of hematopoietic origin.[14] In all tissues where the folate receptors are expressed, the internalization of folate conjugates occurs via a process termed receptor-mediated endocytosis.[15]

The targeted delivery, although successful, implies all drawbacks associated with a long synthetic process, together with a significant cost in term of both time and environmental impact. A possible alternative strategy could be the one in which the folate anion, that acts as recognized agent, is coupled with a species able to exert chemotherapeutic activity and altogether intimately delivered in the cells. In this context, folate based organic salts could be species of interest for a big challenge.

Previous reports in literature have claimed that, different organic cations, like imidazolium and ammonium, bearing long alkyl chain, are able to exert antiproliferative activity towards different cancer cell lines.[16, 17] Consequently, if combined with folate anion, they could represent the active species in the obtaining of folate targeted therapeutic organic salts.

From a chemical point of view, folic acid is also well known for its ability to self-assemble to give hierarchical structures able to organize into high-order structures. To this aim, evidences about the formation of hexagonal or cholesteric phases, in water solution, as a function of concentration have been reported.[18,19] Then, the combination of ammonium or imidazolium ions with folate anion could also offer the possibility to obtain good self-assembling agents.

In the liquid phase, organic salts are able to give highly organized reaction media, also known as ionic liquids, in which the three-dimensional network built by the ions is able to significantly affect the outcome of a reaction.[20-22] On the other hand, in dilute solution, they can act as gelators bringing to the formation of supramolecular gels.[22-24]

Supramolecular gels are semi-solid materials generally obtained from the self-assembly of low molecular weight compounds, also called low molecular weight gelators (LMWGs), or polymeric species. They are featured by the presence of a three-dimensional network, built through the establishment of non-covalent interactions, and able to trap the solvent thanks to the occurrence of supramolecular interactions.[25,26] Supramolecular gels are generally classified on the grounds of the nature of the solvent entrapped and distinguished as hydro-,[27,28] organo-,[29,30] iono-[31,32] and eutectogels,[33,34] if gelled solvents are water, organic solvents, ionic liquids or deep eutectic solvents, respectively. Although the liquid component is predominant, supramolecular gels show the features of a solid material and, during the years, the wide versatility in the gels nature has warranted their application as drug delivery systems, soft materials for environmental reservation and preservation, organized reaction media, sensors and so on.[35-37]

Consequently, in our case, taking in consideration properties of both organic salts and folic acid, we surmised that folate-based organic salts would be able to form supramolecular gels exhibiting

targeted chemotherapeutic activity. To verify this hypothesis, we firstly prepared organic salts differing for the cation structure. In particular, we took in consideration the cholinium folate (**[Ch]$_2$[Folate]**), the *N*-dodecyl-*N*,*N*,*N*-triethylamonium folate (**[$C_{222}C_{12}N$]$_2$[Folate]**) and the 1-dodecyl-3-methylimidazolium folate (**[$C_1C_{12}Im$]$_2$[Folate]**). Comparison between **[Ch]$_2$[Folate]** and **[$C_{222}C_{12}$]$_2$[Folate]** could allow to evaluate the effect deriving from lengthening the alkyl chain on the cation. On the other hand, the comparison between **[$C_{222}C_{12}N$]$_2$[Folate]** and **[$C_1C_{12}Im$]$_2$[Folate]** could give insights about the role played by the different nature of the cationic head (Figure 1).

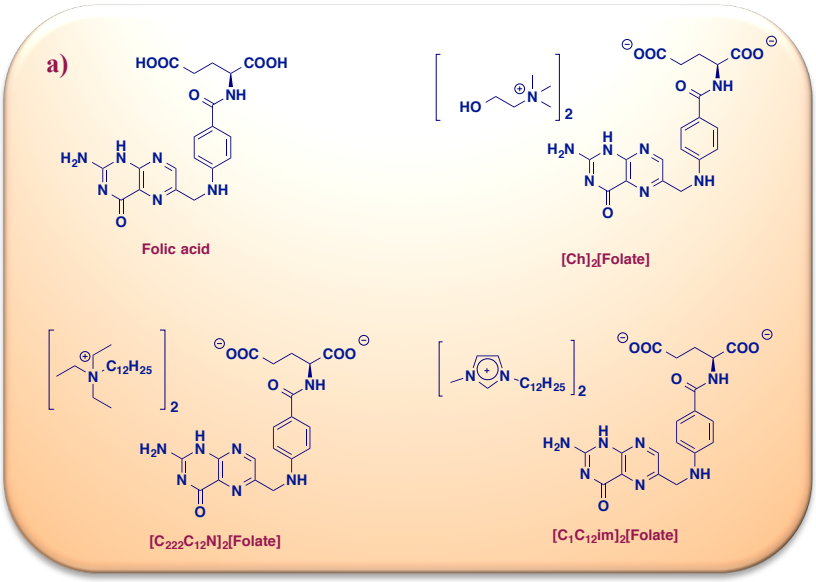

Figure 1. a) Structure of folic acid and folate salts used as gelators; **b)** picture of **[$C_1C_{12}Im$]$_2$[Folate]** gels in PB/DMSO 90/10, TBS and PB, respectively indicated as A, B, C of the picture.

Firstly, we studied photophysical properties of the tested salts, both in biocompatible solvents and solid phase, to obtain information about the occurrence of self-assembly processes. Properties of aggregates were also studied performing dynamic light scattering (DLS) investigation. Then, we performed gelation tests in phosphate buffer (PB), phosphate buffer saline (PBS) and tris-buffered

solution (TBS) and their binary mixtures (90/10; v/v) in the presence of DMSO (PB/DMSO, PBS/DMSO and TBS/DMSO). We observed gelation only in the case of **[C_1C_{12}Im]$_2$[Folate]** and supramolecular gels obtained were fully characterized determining their critical gelation concentration (CGC) and gel-sol transition temperatures (T_{gel}). Furthermore, features of these soft materials were also analyzed, performing ATR-FTIR, rheology, scanning electron microscopy (SEM), resonance light scattering (RLS) and fluorescence investigation. Soft materials were also tested for their ability to respond to the action of external stimuli.

With the aim to investigate the targeting chemotherapeutic activity of the salts, they were tested towards two different human breast adenocarcinoma cell lines, MDA-MB-231 and MCF-7, expressing high and low levels of folate receptor on their surface. Furthermore, we also evaluated the cancer selectivity index (SI), by using the non-tumoral epithelial cell line hTERT RPE-1. The different salt uptake was further analyzed performing tests of antiproliferative activity treating cells with a folate free medium.

As cytotoxicity can be frequently induced by oxidative stress, production of reactive oxygen species (ROS) was determined by dichlorodihydrofluorescein diacetate (DCFH-DA).

Finally, by using one of the best performing soft materials, namely the gel phase formed by **[C_1C_{12}Im]$_2$[Folate]**, in PB/DMSO mixture, we also verified that after the incorporation in the gelatinous matrix, salts were able to exert their biological activity. Data collected evidence that organic salts obtained were able to behave, both in solution and gel phases, as targeted therapeutic agents. Their internalization occurred through a combined mechanism of membrane crossing and receptor-mediated internalization whose contributes depend on the salt structure and cancer cell line nature. The above factors also play a role in determining the observed good selectivity indexes.

Experimental Section

Materials. Folic acid, cholinium chloride, 1-methylimidazole, 1-bromododecane, triethylammine, acetonitrile, Amberlite IRA 400 resin, sodium hydroxide, methanol, hexane, dimethylsulfoxide, glycerol, dioxolane, ethanol, diethyl ether were purchased from commercial sources and used as received. Phosphate buffers (PB) Phosphate buffer saline solutions (PBS) and Tris buffered solution (TBS) were prepared according standardized procedures.

Synthesis of organic salts. Organic salts were synthesized through an anion exchange procedure as previously reported. In particular, the corresponding chloride or bromide salts were exchanged through an anionic resin and using folic acid as source of the new counterion.[16] **[$C_{222}C_{12}N$][Br]** and **[C_1C_{12}Im][Br]** were synthesized following previously reported procedures.[38]

[Ch]$_2$[Folate], yield: 98%. Orange solid. ^{1}H NMR (dmso-d_6) δ (ppm): 1.88 (m, 2H), 2.05 (m, 2H), 3.39 (m, 18H), 3.60 (m, -OH), 3.82 (m, 7H), 4.01 (m, 2H), 4.37 (m, 2H), 6.60 (m, 2H), 6.84 (m, 1H), 7.60 (m, 2H), 8.07 (m, 1H), 8.53 (s, 1H). ^{13}C NMR (dmso-d_6) δ (ppm): 29.2, 34.5, 46.5, 53.6, 55.0, 55.5, 67.5, 111.8, 122.9, 128.7, 128.9, 147.4, 148.2, 150.9, 157.1, 158.0, 164.7, 165.5, 175.2, 175.4, 177.7. Elemental Anal. Calcd. for $C_{29}H_{45}N_9O_8$ (647.73): C, 53.78; H, 7.00; N, 19.46. Found: C, 53.84; H, 6.98; N, 19.42.

[$C_{222}C_{12}N$][Br], yield: 90%. White solid. ^{1}H NMR ($CDCl_3$) δ (ppm): 0.86 (t, J = 9 Hz, 3H), 1.23 (m, 15H), 1.38 (t, J = 9 Hz, 12H), 1.67 (m, 2H), 3.25 (m, 2H), 3.50 (dd, J_1 = 15 Hz, J_2 = 9 Hz, 6H). ^{13}C NMR ($CDCl_3$) δ (ppm): 8.2, 14.2, 22.1, 22.7, 26.5, 29.1, 29.2, 29.3, 29.4, 29.5, 31.9, 53.6, 57.6.

Elemental Anal. Calcd. for $C_{18}H_{39}BrN$ (349.42): C, 61.87; H, 11.25; N, 4.01. Found: C, 61.74; H, 11.22; N, 4.02.

$[C_{222}C_{12}N]_2$[Folate], yield: 95%. Orange powder. ^{1}H NMR (dmso-d_6) δ (ppm): 0.87 (m, 6H), 1.16 (t, J = 6 Hz, 20H), 1.25 (m, 34H), 1.56 (m, 4H), 1.87 (m, 2H), 2.14 (m, 2H), 3.07 (m, 4H), 3.23 (m, 12H), 4.10 (m, 1H), 4.42 (m, 2H) 6.65 (m, 2H), 6.82 (m, 1H), 7.61 (d, J = 6 Hz, 2H), 7.96 (m, 1H), 8.52 (s, 1H). ^{13}C NMR (dmso-d_6) δ (ppm): 7.6, 14.4, 21.4, 22.5, 26.3, 28.9, 29.1, 29.3, 29.4, 29.5, 31.7, 34.1, 52.4, 56.5, 79.6, 111.7, 122.7, 128.8, 146.9, 147.8, 151.1, 165.3, 174.4, 174.6. Elemental Anal. Calcd. for $C_{55}H_{95}N_9O_6$ (978.42): C, 67.52; H, 9.79; N, 12.88. Found: C, 67.41; H, 9.75; N, 12.90.

$[C_1C_{12}Im][Br]$, yield: 89%. Light yellow oil. ^{1}H NMR (dmso-d_6) δ (ppm): 0.85 (m, 3H), 1.24 (m, 20H), 1.77 (m, 2H), 3.85 (s, 3H), 4.15 (t, J = 6 Hz, 2H), 7.72 (s, 1H), 7.79 (s, 1H), 9.17 (s, 1H). ^{13}C NMR (dmso-d_6) δ (ppm): 14.2, 22.7, 26.2, 28.9, 29.3, 29.4, 29.5, 29.6, 30.3, 31.9, 36.8, 50.2, 121.9, 123.7. Elemental Anal. Calcd. for $C_{18}H_{39}BrN$ (331.34): C, 58.00; H, 9.43; N, 8.45. Found: C, 58.11; H, 9.41; N, 8.46.

$[C_1C_{12}Im]_2$[Folate], yield: 93%. Orange waxy solid. ^{1}H NMR (dmso-d_6) δ (ppm): 0.84 (m, 6H), 1.20 (m, 40H), 1.70 (m, 4H),1.86 (m, 2H), 2.08 (m, 2H), 3.95 (m, 1H), 4.11 (t, J = 9 Hz, 6H), 4.36 (m, 2H), 6.58 (d, J = 9 Hz, 2H), 6.76 (m, 1H), 7.55 (d, J = 9 Hz, 2H), 7.69 (s, 2H), 7.75 (s, 2H), 8.22 (m, 1H), 8.48 (s, 1H), 9.35 (s, 2H). ^{13}C NMR (dmso-d_6) δ (ppm): 14.4, 22.6, 25.9, 28.8, 29.2, 29.3, 29.4, 29.5, 29.6, 29.8, 31.7, 36.1, 49.2, 79.7, 111.6, 122.7,122.8, 124.0, 128.7, 128.9, 137.3, 150.9, 165.2, 174.9. Elemental Anal. Calcd. for $C_{55}H_{95}N_9O_6$ (942.26): C, 87.59; H, 3.70; N, 4.32. Found: C, 87.43; H, 3.69; N, 4.33.

Optical measurements in solution and gel phase. UV spectra of gelator in solution (10^{-4} M) of DMSO and in the corresponding gelation solvents were recorded in a quartz cuvette with light path of 0.2 cm. Spectra were recorded from 290 to 550 nm, using a common Beckman Coulter DU 800 spectrophotometer.

Fluorescence measurements were performed on JASCO spectrofluorophotometer using a quartz cuvette with a light path of 0.2 cm in excitation and 1 cm in emission. Solution at a concentration of 10^{-5} M were prepared and spectra were recorded exciting solutions at 280 nm and using excitation and emission width slit both at 2.5 cm.

Fluorescence measurements at variable concentrations were recorded with the above parameters. To this aim, solutions varying from 1 10^{-6} M to 5 10^{-5} M were prepared from stock ones in DMSO at a concentration of 10^{-3} M.

UV-vis and fluorescence measurements in presence of BSA were recorded using the above parameters. Solution of organic salts (10^{-4} M) in PBS in presence of BSA at 2 and 40 μM were prepared for UV-vis measurements, while solution of organic salts (10^{-5} M) in PBS in presence of BSA at 2 and 40 μM were prepared for fluorescence measurements.

The same fluorescence parameters were used to record spectra of gelator hot solution and of the gel formed after storing it in the cuvette at 4 °C overnight.

DLS measurements. Hydrodynamic diameters and polydispersity indexes (PDI) were measured through Malvern Zetasizer NanoZS instrument, equipped with a 632.8 nm laser with the fixed angle of 173°. Organic salts were dispersed in the corresponding water buffer (1.5 10^{-5} M) and

analyzed after syringe filtration (cut-off 5 μm) at 25°C. Measurements were obtained from the average of triplicate samples.

SEM measurements. Scanning Electron Microscopy (SEM) images were recorded on a PRO X PHENOM electronic scanning microscope, operating at 5 kV. 50 mL of organic salts solutions in the corresponding solvents at concentration of $1.5\ 10^{-5}$ M were placed on stubs and the solvent was dried. Gels were placed on the stubs, and the solvent was evaporated to form a xerogel.

Fluorescence quantum yields measurements. Fluorescence quantum yields measurements were carried out in gelation solvents, using an ethanolic solution of 9,10-diphenylanthracene as standard. Concentration of both standard and salt were chosen to have the absorbance of maximum lower or equal to 0.5. The ideal absorbance for fluorescence measurements lies between 0.05 and 0.04, therefore to carry out emission spectra, both standard and sample solution were diluted 10 times. UV–Vis spectra were recorded from 200 nm to 800 nm, while emission spectra from 300 nm to 550 nm, using quartz cuvette with a light path of 0.2 cm in excitation and of 1 cm in emission. Excitation wavelength was chosen in dependence of the solvent used.

Gelation tests and T_{gel} determination. The gelator and solvent (250 mg or 1 g) were weighed in a screw-capped vial of 1 cm or 1.5 cm diameter. The mixture was heated at 80 °C for 1 h, and the resulting solution was stored at 4 °C overnight. Gel formation was determined through the tube inversion test when the solution was not flowing after turning the vial upside down. Gelator concentration varied, starting from 0.2 wt % upon reaching the minimal amount of gelation concentration (CGC).

T_{gel} was determined by the falling drop method.[39] The vial containing the gel was immersed and turned upside down in a water bath, and the bath temperature was gradually increased (2 °C min^{-1}).

The temperature at which the first drop of the gel fell was recognized as T_{gel}. T_{gel} was reproducible within 1 °C.

ATR-FTIR measurements. IR spectra of organic salts and hydrogels were recorded using 16 scans at a resolution of 1 cm^{-1} with a Fourier Transform Infrared Spectrometer (Spectrum One, Perkin Elmer). Measurements were obtained from the average of triplicate samples with a calculated maximum experimental error (relative standard deviation) of around 5%.

Rheology Measurements. Strain and frequency sweep measurements were recorded at room temperature on a TA Instruments (ARES-G2) strain-controlled rheometer using a plate–plate (PP 25-2) tool. The gel was placed between the shearing plates of the rheometer, and each gel was analyzed three times on three different aliquots of the gels. Strain sweep measurements were performed with an angular frequency of 1 rad/s, varying strain from 0.01 to 1000 %, while frequency sweeps were carried out at a fixed oscillation strain of 0.25%, chosen within the viscoelastic region.

Thixotropic and sonotropic behavior. Hydrogels were subjected to the mechanical stimulus, stirring the gel at 1000 rpm for 5 min by using a stirring bar (length=8 mm, height=3 mm) and to the irradiation of ultrasounds, immersing gels in an ultrasound water bath for 5 min with a power of 200 W and a frequency of 45 kHz. Thereafter, the materials were stored at 4 °C overnight.

When the samples were stable to the tube inversion test, gels were defined as thixotropic or sonotropic, respectively.

RLS measurements. RLS measurements were carried out at 20 °C on a spectrofluorophotometer (JASCO FP-777 W) using a synchronous scanning mode. The RLS spectrum was recorded from 300 to 600 nm with both the excitation and emission slit widths set at 1.5 nm. The maximum

intensity of the spectrum obtained was chosen as the working wavelength. Solutions of organic salts, in different gelation solvents, were prepared at concentration below CGC. In the case of gel phase, the limpid hot solution of the gelator was put in the quartz cuvette and it was left to stand at 4 °C overnight. The gel phase formation was assessed by using the tube inversion test and this phase was used to record the RLS spectrum.[40]

Cell lines and culture conditions. The MDA-MB-231 (ATCC® HTB-26™) and the MCF-7 (ATCC® HTB-22™) breast cancer cells and the non-tumoral retinal pigment epithelial hTERT RPE-1 (ATCC® CRL4000™) cell line were cultured in Dulbecco's modified eagle medium (DMEM) (Gibco, Paisley, UK), supplemented with 1% glutamine, 10% heat-inactivated fetal bovine serum and 100U/mL penicillin and 100 µg/mL streptomycin, as already described.[41-43] The cells were maintained at 37 °C in a humidified incubator with 5% CO_2. When the cells were 80% confluent, they were sub-cultured to a fresh media.

Cytotoxicity assay. The cells were seeded at a concentration of 5×10^3 cells/well into a 96-well plate. Following overnight adherence, the cells were incubated with the medium alone (Control) or with a four-fold serial dilution of salts starting with the highest concentration of 100 µM until 0.097 µM for 24 h. Salts were dissolved in DMSO (Sigma, USA) to prepare a master stock solution at the concentration of 1×10^{-2} M and stored at 4 °C until use. The working solutions were freshly prepared in the complete culture medium. Then, 20 µL Thiazolyl Blue Tetrazolium Bromide (5 mg mL−1) in PBS was added to each well and mixed. After 2 h, the supernatants were removed and 100 µL of DMSO was added to each well to dissolve the precipitate. The cells viability was estimated by measuring absorbance at 570 nm using a microplate reader (Spark® 20M Tecan Trading AG, Switzerland), as previously reported.[44] The cell viability percentage was calculated based on the average of absorbance ratio between treated and untreated cells multiplied by 100,

after subtraction of the blank. The IC_{50} values, that is the concentration necessary to inhibit the 50% of cell growth, was calculated using a dose-response model, obtained from sigmoidal fitting of response curves of percent inhibition versus logarithmic concentration of salts, using Graph Pad Prism software. Each result represents the mean value of three different experiments performed in triplicate ±SD.

Cancer Selectivity Index (CSI) was calculated as the ratio of cytotoxicity (IC_{50}) on normal cells (hTERT RPE-1) to cancer cells (MDA-MB-231 and MCF-7). The CSI value higher than 3 suggested that the cytotoxic effect of salts was selective towards MCF-7 cells and MDA-MB-231[45, 46]

Treatment of MCF-7 and MDA-MB-231 cells with Folate salts and gel and morphological assessment. MDA-MB-231 and MCF-7 cells were seeded in a 6 or 48-well plate at 12×10^3 and 20×10^3 cells/cm^2 and allowed to attach for 24 h. Then, the cells were incubated with the different concentration of folate salts, or with **$[C_1C_{12}Im]_2$[Folate]** in gel phase from TRIS/DMSO (90/10) at 6 wt %, gelled on a coverslip or with appropriately dilutions of the gelator released from **$[C_1C_{12}Im]_2$[Folate]**-derived gel immersed in 20 ml of DMEM and picked up after 24h, 48h, 72 h and 96 h for different times point. Cells were observed under a fluorescence or a phase contrast inverted microscope (Carl Zeiss AG, Oberkochen, Germany) at 100X or 200Xmagnification, using DAPI, FITC filters or transmitted light.

Evaluation of ROS generation. Intracellular ROS levels were measured by using 2′,7′-dichlorodihydrofluorescein diacetate (DCFHDA), a cell-permeable probe, routinely used to measure intracellular generation of H_2O_2 and other oxidants; MDA-MB-231 and MCF-7 cells were plated in 96 well plates at a density of 5×10^3 /well, allowed to growth overnight and incubated

for 24 h with different Folate salts concentrations. At the end the medium was replaced with the culture medium containing DCFH-DA (10μM) and incubated for 30min at 37 °C. Then the medium was replaced with PBS and the fluorescence intensity was analyzed by spectrofluorimeter with an excitation of 488 nm and emission wavelength of 525 nm. Data normalization was performed with parallel MTT assay.

Results and Discussion

Photophysical properties of the salts. To have insights on the photophysical behavior of the folate organic salts, we firstly analysed the emission behavior of their solutions (10^{-4} M), under irradiation at 365 nm. To this aim, DMSO solutions, aqueous buffer solutions and their binary mixtures with DMSO were compared (Figure 2).

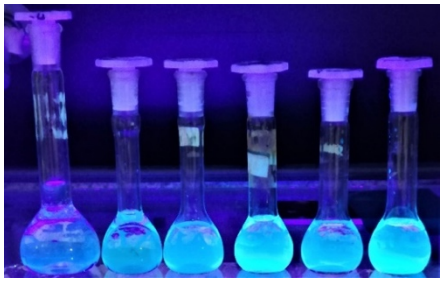

Figure 2. Solutions irradiated at 365 nm, from left to right: folic acid in H_2O/DMSO (50:50), **[C_1C_{12}Im]$_2$[Folate]** in DMSO, **[C_1C_{12}Im]$_2$[Folate]** in PBS/DMSO (90/10), **[C_1C_{12}Im]$_2$[Folate]** in PBS, **[C_1C_{12}Im]$_2$[Folate]** in PB/DMSO (90/10), **[C_1C_{12}Im]$_2$[Folate]** in PB.

In all cases, more significant fluorescence emission was detected in the binary mixtures or in buffer solutions than in DMSO. The above evidence allowed supposing that increasing the solvent polarity, on going from DMSO to aqueous buffers, favored the occurrence of self-assembly processes, giving rise to the formation of emissive aggregates. On the grounds of the above

hypothesis, we firstly recorded UV-vis spectra of folic acid and the corresponding salts in DMSO solution (Figure 3a).

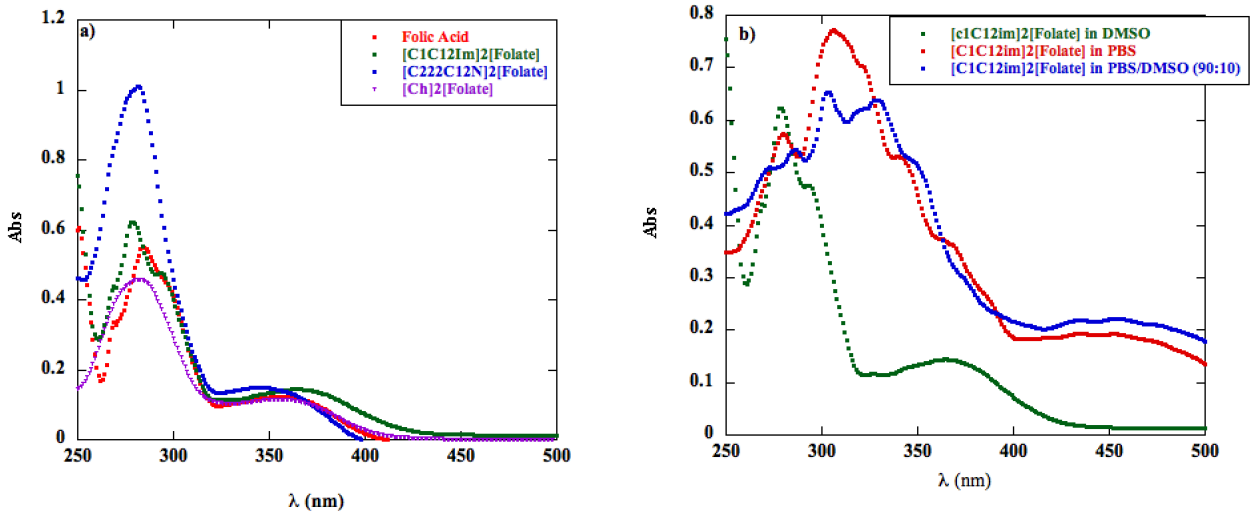

Figure 3. UV spectra of: **a)** folic acid and organic salts in DMSO at $1 \cdot 10^{-4}$ M; **b)** **[C_1C_{12}Im]$_2$[Folate]** in DMSO, PBS and PBS/DMSO (90/10) at $1 \cdot 10^{-4}$ M.

Analysis of obtained spectra evidences the changes that can be detected on going from folic acid to corresponding salts, as a function of the nature of the cation. Indeed, in DMSO solution, folic acid showed a main absorption band centered at 284 nm. **[C_1C_{12}Im]$_2$[Folate], [$C_{222}C_{12}$N]$_2$[Folate]** and **[Ch]$_2$[Folate]** exhibited hypsochromic shift of the main absorption bands at 278 nm (**[C_1C_{12}Im]$_2$[Folate]** and **[Ch]$_2$[Folate])** and 281 nm (**[$C_{222}C_{12}$N]$_2$[Folate]**).

On the grounds of the above result, among the salts, we payed particular attention to **[C_1C_{12}Im]$_2$[Folate]**, that showed the largest variation in λ_{Max} and the ability to form gel phases (see later). For this salt, we recorded UV-vis spectra changing the nature of the solvent and increasing both polarity and ionic strength of the solutions, using DMSO, PBS/DMSO and PBS (Figure 3b).

Analysis of the spectra evidences that adding PBS to DMSO solution induced a significant batochromic shift in the main absorption band. Indeed, its position moved from 278 nm, in DMSO, to 302 and 305 nm in PBS/DMSO and PBS. A similar behavior has been previously reported in literature, studying both the self-assembly process of dendritic oligo (L-or D-glutamic acid) moieties of folic acid[47] and the gelling ability of folic acid in different DMSO/water binary mixtures.[48] In both cases, the batochromic shift, induced by the increase in solvent polarity, was ascribed to the occurrence of a self-assembly process, driven by π–π interactions and giving rise to the formation of *J*-aggregates, in which ptering rings of the chromophore were twisted.[49-51] However, in our case, the above behavior shows a buffer nature dependency. Indeed, changing PBS with PB, less significant changes were detected and λ_{MAX} moved from 278 in DMSO to 281 nm, in PB, and 276 nm in PB/DMSO. Finally, the use of TBS did not induce variation (Figure S1).

A further support to the occurrence of aggregation process also derived from the shape of the absorption band. Indeed, a clear fine structure was observed in DMSO solution, accounting for the predominance of the monomeric form. Differently, the above information was almost lost in PBS and partially also in PBS/DMSO mixture, accounting for the presence of aggregates. A similar behavior has been previously reported in literature, comparing UV-vis spectra of folic acid in *N*-methylpyrrolidone/H_2O solution and gel phase and it was ascribed to the existence of π-π interactions.[52]

To analyze the behavior of the tested organic salts in a more hydrophobic environment, in the light of their possible application as antiproliferative agents and with the aim to mimick the cellular membrane environment, we recorded UV-vis and emission spectra of organic salts in the presence of Bovine Serum Albumine (BSA). BSA is a transport protein and it is considered as the most

abundant water-soluble protein. It is able to bind and act as carrier of fatty acids, anions and other small amphiphiles in bloodstreams.[53] Furthermore, it has been demonstrated that BSA has considerably high binding affinity for a wide range of small molecules.[54,55] Consequently, in our case, it could be a suitable system to verify if the interaction with the cellular environment involved the single folate ion or the ion pair.

To this aim, we recorded both UV-vis and emission spectra, at fixed concentration of salts ($1.2 \cdot 10^{-4}$ and $1.2 \cdot 10^{-5}$ M, respectively) and in the presence of increasing amounts of BSA (2 and 40 μm; Figure S2 and S3).

As far as Uv-Vis spectra are concerned, the first effect we observed on the absorption band centered at ~ 350 nm was an hypsochromic shift that was more significant in the case of **[Ch]$_2$[Folate]** and **[$C_{222}C_{12}N$]$_2$[Folate]** and depended on BSA concentration (Table S1). Furthermore, in the above cases, significant changes in the absorbance values were detected at 364 nm. In general, absorbance values were affected by the cation nature.

The above behavior was also detected as far as emission spectra were concerned. Indeed, analysis of the emission band centered at ~ 440 nm, showed different emission intensity values as a function of the cation nature (Table S2), indicating that diffusion from hydrophilic to hydrophobic environment pertained the whole ion pair.

Bearing in mind the significant increase in fluorescence emission (Figure 2), observed upon the adding of aqueous buffer to DMSO and the relevant changes in the position of the main absorption band, PBS was chosen as model solvent and fluorescence spectra of all tested organic salts were recorded as a function of concentration in the range $1 \cdot 10^{-6} \div 5 \cdot 10^{-5}$ M. We tried to perform the

same investigation in the case of folic acid, but the low solubility in PBS did not allow to obtain reproducible results.

Superimposed fluorescence spectra obtained in the case of **[$C_1C_{12}Im]_2$[Folate]** are reported in Figure 4, together with the trend of emission intensity as a function of salt concentration.

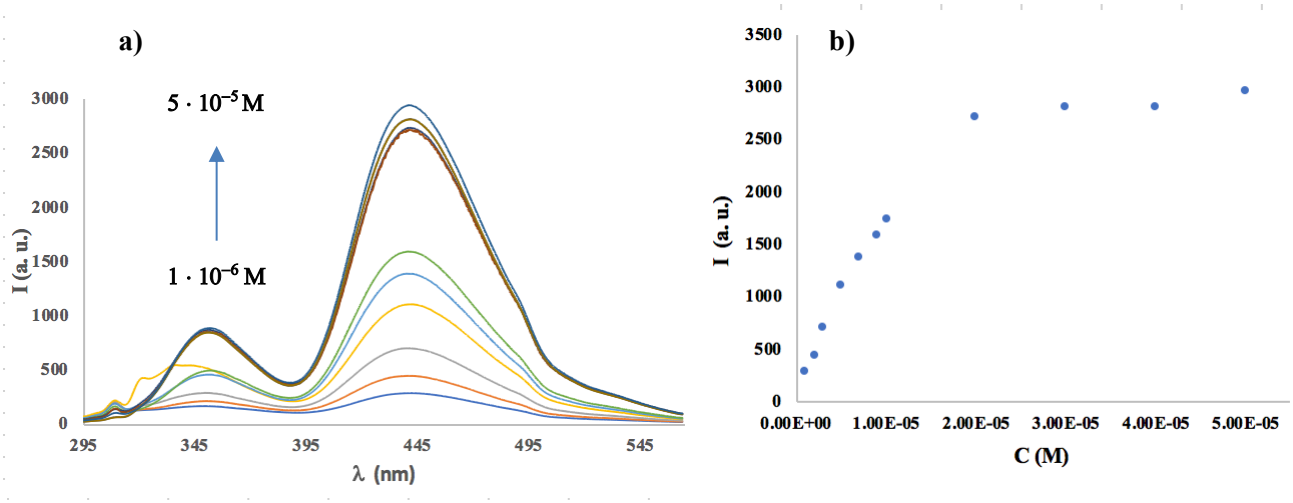

Figure 4. a) Fluorescence spectra of **[$C_1C_{12}Im]_2$[Folate]** in PBS at variable concentrations; **b)** fluorescence intensity at 440 nm as function of salt concentration.

Spectra corresponding to **[$C_{222}C_{12}N]_2$[Folate]** and **[Ch]$_2$[Folate]** are reported in Figure S4. Fluorescence spectra were in all cases featured by the presence of two emission bands. The first one of lower intensity centered at ~ 350 nm and the second one of higher intensity located at ~ 440 nm. According to previous reports in literature, the above emission bands can be ascribed to n-π* and π-π* transitions, respectively.[56,57]

In all cases, emission intensity, at 440 nm, increased as a function of salt concentration until a constant value was reached, giving rise to a hyperbolic trend. The non-monotonic trend obtained was indicative, in all cases, of the occurrence of self-assembly processes that gave rise to the formation of aggregates more emissive than the corresponding monomers. In the case of **[C_1C_{12}Im]$_2$[Folate],** this information, together with the one related to the bathochromic shift of the main absorption band, detected as a consequence of the increase in solvent polarity, allowed definitively ascertain the presence of *J*-aggregates.[57]

Determination of the change in slope in the hyperbolic trend allowed calculating the aggregation concentration (C_{agg}), *i.e.* the minimum concentration of salt needed for the aggregates formation. The above parameter changed as a function of the nature of the salt and was equal to 1.50, 1.90 and 1.55 · 10^{-5} M, in the case of **[Ch]$_2$[Folate]**, **[$C_{222}C_{12}$N]$_2$[Folate]** and **[C_1C_{12}Im]$_2$[Folate]**, respectively (Figure S5).

A first comparison between **[Ch]$_2$[Folate]** and **[$C_{222}C_{12}$N]$_2$[Folate]** sheds light on the role played by the presence of hydroxyl group on the side chain of the cation. Probably, as a consequence of the establishment of hydrogen bonds, it favors the occurrence of aggregates formation at a lower concentration with respect to the salt bearing a longer and more flexible alkyl chain (**[$C_{222}C_{12}$N]$_2$[Folate]**). Furthermore, this latter, as a consequence of a higher conformational flexibility, could make more difficult the self-assembly process. We detected a similar behavior, studying the self-assembly process of naphtalenediimide-based organic salts as a function of the alkyl chain length borne on the cationic head.[20]

On the other hand, in the presence of a dodecyl chain, the aliphatic or aromatic nature of the charged head seems to play a role, as shown by the decrease in C_{agg} detected on going from

[$C_{222}C_{12}N$]$_2$[Folate] to **[C_1C_{12}Im]$_2$[Folate]**, accounting for a higher self-assembling ability for the aromatic cation with respect the aliphatic one.

Interestingly, analysis of the largest variation in fluorescence intensity (ΔI), as a function of the salt concentration, gave the following trend: **[$C_{222}C_{12}N$]$_2$[Folate]** < **[Ch]$_2$[Folate]** < **[C_1C_{12}Im]$_2$[Folate]** (ΔI = 1640, 2061 and 2670 a.u., respectively), indicating supramolecular aggregates formed by **[C_1C_{12}Im]$_2$[Folate]** as the most fluorescent ones.

To better explain the above result, we measured the fluorescence quantum yield ($\Phi_{F(x)}$) in ethanol, using 9,10-diphenylanthracene as standard ($\Phi_{F(x)}$= 0.95) in ethanol.[58] Superimposed emission spectra of salts are reported in Figure S6. $\Phi_{F(x)}$ was calculated according to eq. (1), previously reported in literature:[59]

$$\Phi_{\mathrm{F(x)}} = \left[\left(\frac{As}{Ax}\right) \cdot \left(\frac{Fx}{Fs}\right) \cdot \left(\frac{nx}{ns}\right)^2\right] \cdot \Phi_{F(s)} \qquad \text{eq. (1)}$$

where A represents the absorbance of solution at the excitation wavelength, F is the integrated band area, *n* represents the refraction index of solvent and x and s refer to sample and standard, respectively. $\Phi_{F(x)}$ values are reported in Table 1.

Table 1. Relative emission quantum yields of organic salts, at $2 \cdot 10^{-5}$ M in ethanol solution, determined using 9,10 diphenylanthracene as reference.

Fluorophore	$\Phi_{F(x)}$
9,10 diphenylanthracene	0.95
[Ch]$_2$[Folate]	0.24
[$C_{222}C_{12}N$]$_2$[Folate]	0.17
[$C_1C_{12}Im$]$_2$ [Folate]	0.44

Analysis of the obtained values evidences that the emission quantum yield increases along the following trend: **[$C_{222}C_{12}N$]$_2$[Folate] < [Ch]$_2$[Folate] < [$C_1C_{12}Im$]$_2$[Folate]**, perfectly accounting for the emission variations detected as a consequence of the aggregates formation.

Taking in consideration the above information, indicating the marked tendency of **[$C_1C_{12}Im$]$_2$[Folate]** to form aggregates also supported by its gelation ability (see later), we performed DLS investigation using its solutions ($1 \cdot 10^{-4}$ M) in different aqueous buffers and buffer/DMSO mixtures (Figure S7 and Table S3).

Analysis of data reported in Table S3 demonstrate that the hydrodynamic diameter (d_H) ranged from ~ 650 nm (PDI = 0.55), in PB solution, up to 980 nm (PDI = 0.67) in PBS/DMSO solution. This parameter was affected by the nature of the buffer used, increasing on going from PB to TBS. Addition of DMSO induced different effects in dependence on the nature of the buffer. Indeed, an increase in d_H values was observed when DMSO was added to PB and PBS, whereas a decrease in the same parameter was detected in the case of TBS solution.

Finally, organic salts were also investigated for their ability to give fluorescence emission in the solid state. This property could be of a certain interest, as one of the main aims of the present work was the investigation of their gelling ability and, gel phases are classified as semi-solid materials.

To this aim, we deposited 1 mL of a PBS solution of salt, at a concentration higher than C_{agg} ($3 \cdot 10^{-5}$ M), on a quartz disk and evaporated the solvent in the air. This allowed us to have a thin layer of aggregates to record emission spectra. Superimposed emission spectra recorded in solution and in solid phase, corresponding to **[C_1C_{12}Im]$_2$[Folate]**, are reported in Figure 5, whereas the ones corresponding to **[Ch]$_2$[Folate]** and **[$C_{222}C_{12}$N]$_2$[Folate]** are displayed in Figure S8.

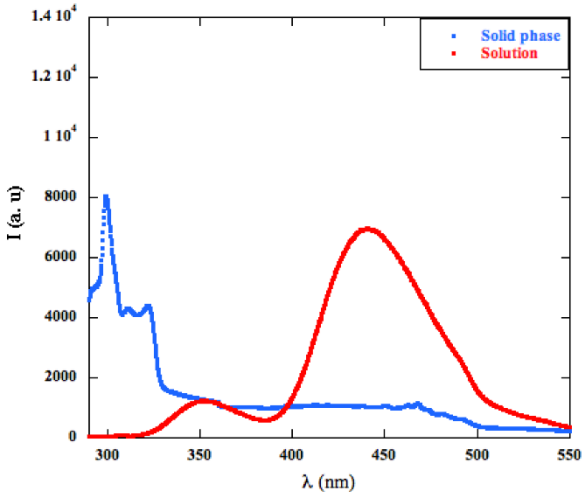

Figure 5. Superimposed fluorescence spectra, in PBS solution ($3 \cdot 10^{-5}$ M) and solid phase, for **[C_1C_{12}Im]$_2$[Folate]**.

In all cases, we detected a significant fluorescence emission also in the solid state, with a clear hypsochromic shift of the main emission band. The observed blue shift in solid state has been frequently observed in strong emitters with the so-called "aggregation-induced emission"

behaviour and has been ascribed to restrictions occurring in the geometry of the excited state, that induce its planarization and freezing.[60-63]

Gelation properties. Taking in consideration the biological aim of the present work, gelation tests were performed in biocompatible solvents like, water, PB, PBS and TBS, also in combination with DMSO (Table S4). Tests were carried out by heating the proper amount of gelator and solvent, at 80 °C for 1h, then the hot solution was stored overnight at 4 °C. Gel phase formation was assessed by using the tube inversion test.[64] For a useful comparison, tests were also performed by using folic acid. Table 2 displays critical gelation concentration values (CGC), *i.e.* the lower amount of gelator needed to have gel phase formation, and temperatures corresponding to gel – sol transition (T_{gel}).

Table 2. CGC and T_{gel} values of gels for Folic acid and **[$C_{222}C_{12}$Im]$_2$[Folate]** as a function of the solvent.

		Folic acid		**[C_1C_{12}Im]$_2$[Folate]**	
Entry	**Gelation solvent**	**CGC(wt. %)**[b]	T_{gel} **(°C)**[c]	**CGC(wt. %)**[b]	T_{gel} **(°C)**[c]
1	H_2O/DMSO (50/50)[a]	0.2%	46.0	/	/
2	TBS	/	/	4.0%	43.0
					[*]48.7
3	TBS/DMSO (90/10)[a]	/	/	5.5%	[*]43.5
4	PB	/	/	4.0%	59.2
					[*]63.2
5	PB/DMSO (90/10)[a]	/	/	4.0%	65.0
					[*]64.6
6	PBS	/	/	5.0%	40.3
					[*]67.7
7	PBS/DMSO (90/10)[a]	/	/	6.0%	[*]54.8

*[a]volume ratio (v/v); [b]=critical gelation concentration (g gelator/g solution); [c]=temperature of gel-solution transition, reproducible within 1 °C, determined with the falling drop method. *T_{gel} determined at 6 wt % (g gelator/g solution).*

Aliphatic organic salts, **[Ch]$_2$[Folate]** and **[C$_{222}$C$_{12}$N]$_2$[Folate]**, were soluble in most of buffers and binary mixtures, prepared in the presence of DMSO, precluding the obtainment of gel phases (Table S4).

Differently, folic acid and **[C$_1$C$_{12}$Im]$_2$[Folate]** were insoluble in water and soluble in DMSO. This is the reason why mixtures, at variable percentage, of these solvents were prepared for gelation tests. According to previous report in literature, folic acid was able to gel only in H_2O/DMSO (50/50; v/v) binary mixture, at very low concentration (0.2 wt %), acting as a supergelator.[65] Conversely, **[C$_1$C$_{12}$Im]$_2$[Folate]** gelled in TBS, PB and PBS also in combination with DMSO at 10% in volume. However, CGCs for **[C$_1$C$_{12}$Im]$_2$[Folate]** were higher than the one corresponding to folic acid, ranging from 4 up to 6 wt%.

The above results, indicate that on going from folic acid to the corresponding conjugate salts, a gradual decrease in gelation ability can be detected. Furthermore, the above behavior is significantly affected by the nature of the cation of the organic salts, as accounted for by the disappearance of the gelling ability going from **[C$_1$C$_{12}$Im]$_2$[Folate]** to **[C$_{222}$C$_{12}$N]$_2$[Folate]**, notwithstanding the comparable hydrophobicity of the dodecyl chain borne on the cation.

Analysis of these results provide insights on the nature of the interactions working in the formation of the gelatinous network. Indeed, the very low CGC detected in the case of folic acid probably accounts for the prominent role played by hydrogen bond. In addition, a lower relevance of hydrophobic effects can be expected on going from neutral folic acid to the relevant salts. Substitution of acid with the corresponding conjugate base and, consequently, the use of gelators less prone to donor hydrogen bond, gives rise to the obtainment of a less efficient gelator (**[C$_1$C$_{12}$Im]$_2$[Folate]**) or a non gelator (**[C$_{222}$C$_{12}$N]$_2$[Folate]**). Furthermore, the substitution of the

aromatic cation ($[C_1C_{12}Im^+]$) with the aliphatic one ($[C_{222}C_{12}N^+]$), completely suppresses the gelation ability, indicating that π–π interactions that can be established between electron deficient imidazolium and electron rich folate ion, belonging to different ion pairs, are more efficient in building of the tridimensional network, with respect to cation-π interaction that can act in the case of **$[C_{222}C_{12}N]_2$[Folate]**.

In the case of **$[C_1C_{12}Im]_2$[Folate]**, gelation ability was also affected by the nature of the solvent. Indeed, with the only exception of PB/DMSO mixture, the addition of DMSO to the buffer solution induced a significant increase in the CGC value, accounting for a decrease in the gelation ability.

Probably, DMSO caused a destabilizing effect in salt gelling ability interfering with supramolecular interactions operating in buffer solution (4 to 5.5 wt% for gel in TBS and TBS/DMSO and 5 to 6 wt% for PBS and PBS/DMSO).

To have further insights about the interactions working in the building tridimensional network of gel phase, ATR-FTIR investigation was carried out. Figures S9 and S10 display ATR-FTIR spectra of organic salts and gel phases formed by **$[C_1C_{12}Im]_2$[Folate]**. In the case of organic salts, main bands correspond to stretching of N-H groups of folate ion at 3300-3400 cm^{-1}. The above bands can be clearly identified in the case of **$[C_{222}C_{12}N]_2$[Folate]** and **$[C_1C_{12}Im]_2$[Folate]**, whereas in the case of **$[Ch]_2$[Folate]** the above signal is superimposed to the one of hydroxyl group of cholinium cation. Furthermore, also the signal corresponding to the stretching of C=O group of secondary amide function of folate anion at 1686 cm^{-1} can be detected. Small differences in the frequency values corresponding to symmetric and asymmetric stretching of carboxylate groups can be detected as a function of cation nature. The above frequency changed from 1604 and 1393 cm^{-1} for

[$C_{222}C_{12}N$]$_2$[Folate] to 1563 and 1375 cm^{-1} in the case of **[Ch]$_2$[Folate] and [C_1C_{12}Im]$_2$[Folate]**, accounting for the occurrence of cation-anion hydrogen bond interactions.

Going from **[C_1C_{12}Im]$_2$[Folate]** to the corresponding gel phases, we did not observe significant differences in the above frequency values. According to previous hypothesis, this indicates the high relevance of π-π interactions in the building of the gelatinous network.

Gel phases were also analyzed for their thermal stability. To this aim, gel-sol transition temperature, T_{gel}, was determined with the falling drop method.[39] T_{gel} were assessed both at the CGC and by using a common concentration equal to 6 wt % (Table 2).

At the CGC, T_{gel} ranged from 43 up to 65 °C. Once again, solvent nature plays a role in determining the trend of the above parameter. Indeed, notwithstanding equal CGC values collected in TBS and PB, T_{gel} significantly increased going from TBS to PB. This trend is maintained also for gels at 6 wt %.

Keeping constant the gelator concentration, allows to collect some other interesting insights. Indeed, the increase in ionic strength, going from PB to PBS, induces a corresponding increase in T_{gel} value. The addition of DMSO to the buffer solutions, in two of three cases (TBS and PBS), induced a significant increase in thermal stability of the gel, indicating that the presence of the cosolvent moves the CGC at higher values, but favors the formation of gels melting at higher temperature.

Rheology measurements. To have information about the features of gel phases, they were analyzed for their mechanical behavior. To this aim, both strain and frequency sweep measurements were performed at 25 °C. In particular, gel phases formed in aqueous buffers at 6 wt % were taken in

consideration, together with the one formed in PB/DMSO, to analyse the effect exerted by the cosolvent on the mechanical properties of the gels.

Strain sweeps were carried out at ω = 1 rad/sec, whereas frequency sweeps were carried out by using a strain value equal to 0.25%. Plots of *G'* and *G''* as a function of strain or frequency values are reported in Figures 6 and S11.

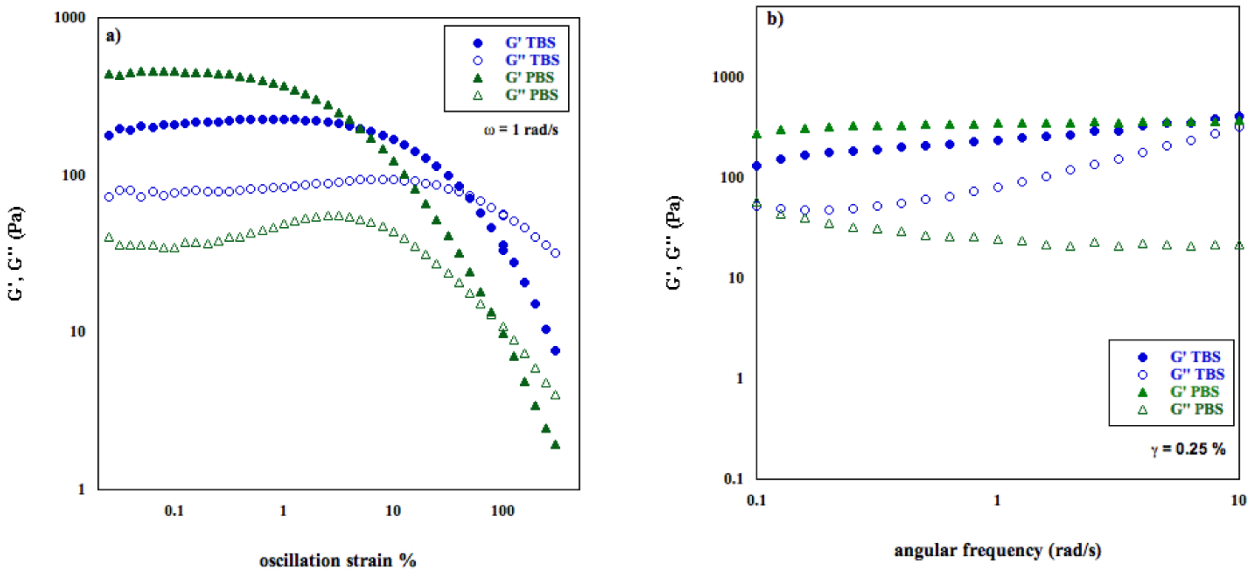

Figure 6. Strain and frequency sweeps of hydrogels formed by **[C_1C_{12}Im]$_2$[Folate]**, in TBS and PBS at 6 wt %.

In the strain sweeps, at low strain values, *G'* was always higher than *G''*, until a certain value (γ_c), corresponding to the moduli inversion. This behavior is the typical one detected for a gel phase. On the other hand, according to the above evidence, in the frequency sweep measurements, *G'* was always higher than *G''* and both moduli were independent from the frequency values.

Analysis of the above trends allows the obtainment of important rheological parameters, like G' and G'' that represent the storage and the loss moduli, respectively, and give an idea about the strength of the gel phases. On the other hand, also the tangent loss ($\tan\delta = G''/G'$) and the cross-over point (γ_c) can be determined. The first parameter allows the evaluation of the forces operating in the gel network. In general, the lower is this value, the higher is the intensity of such kind of forces. On the other hand, γ_c represents the amount of strain that must be applied to induce the gel network breakdown. All the above parameters are reported in Table 3.

Table 3. Rheological parameters for **[$C_1C_{12}Im]_2$[Folate]** gels determined at 25 °C, γ = 0.25 % and ω = 1 rad/sec. Values determined as average values on three different aliquots of gels.

Gelation solvent	G' (Pa)	G'' (Pa)	tanδ	γ_c (%)
TBS	210±30	80±3	0.39±0.06	40±10
PBS	393±71	31±10	0.11±0.05	95 ±5
PB	560±130	140±70	0.25±0.07	39.66±0.03
PB/DMSO	1073±35	450±120	0.40±0.08	9±1

Analysis of above values allows drawing some interesting considerations. In particular, all gel phases are featured by the occurrence of strong colloidal forces, as accounted for by tanδ values significantly lower than 1. The highest intensity of colloidal forces was detected in PBS-based gel and this was also supported by the very high value measured for γ_c.

In general, the decrease in ionic strength, going from PBS to PB, induced the formation of a less strong gel phase, as accounted for by the increase in tanδ and decrease in γ_c values. A further significant decrease was also detected as a consequence of DMSO addition to gelation solvent. On the other hand, for solvents having higher ionic strength, PBS and TBS, also the nature of the buffer affects rheological features, as testified by the significant increase in tanδ and decrease in γ_c values, going from PBS to TBS.

Interestingly, all the above trends perfectly recall the ones above discussed about T_{gel}, evidencing the parallelism between thermal stability and mechanical features.

Morphology. Gel phases were also analyzed for their morphology by using SEM investigation. In particular, soft materials formed in PB, PBS and PB/DMSO, at 6 wt %, were taken in consideration (Figure 7).

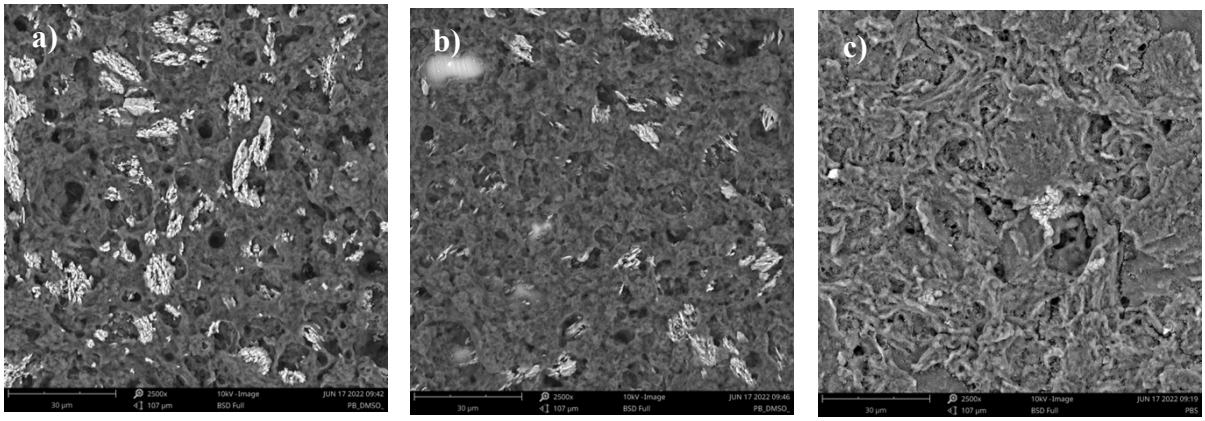

Figure 7. SEM images corresponding to gel phases formed by **[C_1C_{12}Im]$_2$[Folate]** in: a) PB; b) PBS and c) PB/DMSO.

Analysis of collected images evidences that morphology is slightly affected by the solvent nature. Basically, in all cases, the morphology is fibrous in nature. However, going from PB to PB/DMSO to PBS, an increase in the density of the texture can be detected. Furthermore, PB-based gel exhibits the presence of several crystallite-like structures sprinkled in the gelatinous network, that decrease in PB/DMSO.

Self-healing ability. Gel phases were also tested for their ability to respond to the action of external stimuli. In particular, thixotropic and sonotropic behavior were taken in consideration, to verify if they were able to reform after disruption induced by magnetic stirring or ultrasound irradiation (see Experimental). Results collected are displayed in Table 4.

Table 4. Results of sonotropy and thixotropy tests of corresponding gels.

Gel	Sonotropy	Thixotropy
$[C_1C_{12}Im]_2$[Folate] in TBS	STABLE	YES
$[C_1C_{12}Im]_2$[Folate] in TBS /DMSO	NO	YES
$[C_1C_{12}Im]_2$[Folate] in PB	STABLE	YES
$[C_1C_{12}Im]_2$[Folate] in PB /DMSO	STABLE	YES
$[C_1C_{12}Im]_2$[Folate] in PBS	STABLE	YES
$[C_1C_{12}Im]_2$[Folate] in PBS /DMSO	STABLE	YES
Folic acid in H_2O/DMSO (50/50)	STABLE	YES

In general, all gel phases showed thixotropic behavior as they were destroyed by magnetic stirring, but they were able to reform after rest at room temperature. Conversely, with the only exception of gel formed in TBS/DMSO, all gel phases were not affected by ultrasound irradiation, generally proving stable.

Resonance Light Scattering and Fluorescence Investigation. To have further insights about aggregates featuring gel phases, Resonance Light Scattering (RLS) was performed both at concentration below and above CGC.

RLS is a technique that allows to gain information about the size of aggregates formed by chromophores.[66] It has been widely used to study porphyrins-based systems, but also ionic liquids[38] and gel phases.[23,67] This technique proves very useful as it allows to have information about the size of the aggregates. Indeed, RLS intensity (I_{RLS}) can be related to the above parameter and increases with the size of aggregates.[68] Consequently, the versatility of this technique well supports the investigation in self-assembling systems that can give rise to the formation of gel phases.

With the above considerations in mind, we firstly analysed **[C_1C_{12}Im]$_2$[Folate]** solutions ($2.6 \cdot 10^{-4}$ M), in different buffers and buffer/DMSO binary mixtures. RLS spectra are reported in Figure 8 and S12. I_{RLS} values detected at 450 nm are reported in Table 5.

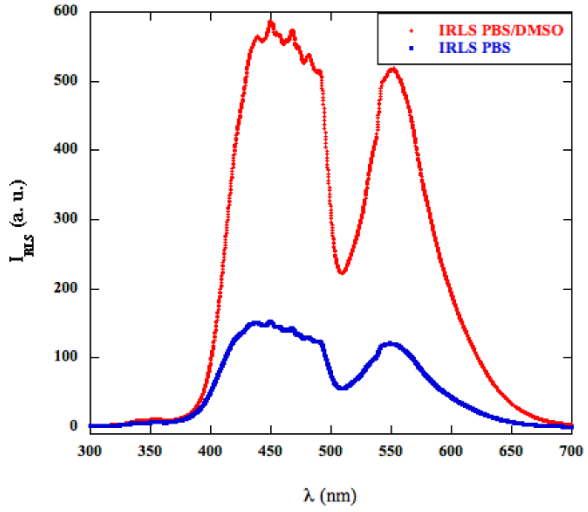

Table 5. I_{RLS} at 450 nm

Solvent	I_{RLS} (450 nm)
PBS	150
PBS/DMSO	580
TBS	1520
TBS/DMSO	500
PB	250
PB/DMSO	320

Figure 8. RLS Spectra of **[C_1C_{12}Im]$_2$[Folate]** solution in PBS and PBS/DMSO ($2.6 \cdot 10^{-4}$ M). I_{RLS} at 450 nm, for different solutions at 450 nm, are displayed in Table 5.

Analysis of the above data evidences how, in clear proximity region, the size of the aggregates increases along the following trend: PBS < PB < TBS, highlighting a significant effect deriving from the solvent nature on the aggregation process.

In two of three cases, PBS and PB, the addition of DMSO induced a significant increase in the size of the aggregates. Conversely, in TBS solution, DMSO addition caused the aggregates breaking up and, in the binary mixtures, I_{RLS} increases along the order: PB/DMSO < TBS/DMSO < PBS/DMSO. The above result perfectly agrees with data previously discussed about DLS investigation (see above).

We also performed RLS investigation on gel phases, at 6 wt % in buffer and buffer/DMSO binary mixtures. RLS spectra are reported in Figure S13. I_{RLS} values, at 470 nm, are reported in Table S5. In general, gel phases formation induced the occurrence of quite extended aggregates. In aqueous buffer, I_{RLS}, at 470 nm, decreases going from PB to TBS, evidencing that the size of the aggregates heavily depends on the nature of the gelation solvent (Table S5). The above trend is different from the one detected in the case of aggregates solution. Furthermore, for gels, independently from the buffer nature, DMSO addition to gelation solvent caused a significant decrease in the size of the aggregates.

Taking in consideration that size and aggregates organization play a significant role in determining properties of gel phases, we tried to correlate RLS data with mechanical properties and morphology of soft materials. Similarly, to RLS data, tanδ values decrease going from TBS to PB. The above trend indicates that gel phases featured by more extended aggregates also have higher stiffness. Furthermore, DMSO addition (PB/DMSO) causes a significant decrease in the size of

the aggregates that has relevant consequences on both tanδ and γ values. Indeed, gel formed in PB/DMSO shows a lower stiffness and need the application of a lower strain to be broken down.

Interestingly, the above features well correlate also with gel phases morphology. Indeed, PB-based gel, featured by the occurrence of more extended aggregates and better mechanical properties than PB/DMSO gel, exhibit a fibrous texture with more crystallite structures with respect to the one observed in the case of PB/DMSO gel (Figure 7).

Finally, we also recorded fluorescence spectra for the hot solutions and corresponding gel phases, with the aim to understand the effect of aggregation on the emission behavior of tested organic salts. In general, no significant differences were observed going from the hot solution to the corresponding gel phases, probably because of the fast gelation process. Emission spectra for gel phases are reported in Figure S14, together with the picture of gels irradiated at 365 nm. In general, emission intensity of gel phases, in aqueous buffers, was not very high and proved significantly lower than the one detected for corresponding gelator in dilute solution, indicating that the formation of the tridimensional network induced a quenching of the fluorescence emission.

Anticancer activity of Folate salts. To understand how changes in the salts structure affect their activity, they were tested towards two human breast adenocarcinoma cancer cell lines, MDA-MB-231 and MCF-7, expressing high and low levels of folate receptor (FR) on their surface.[69-72]

In a first attempt, considering the photophysical behavior of folate organic salts, cellular imaging was investigated by fluorescence microscopy. However, no fluorescence was detected inside the cells, even with high doses (up to 20 μm for 24h) for **$[C_{222}C_{12}N]_2$[Folate]** and **$[C_1C_{12}Im]_2$[Folate]**.

The cell viability was measured by MTT assay after 24 h of incubation, using different concentrations of folate salts. The activity of the salts was compared with the one of the corresponding halide salts (**[$C_{222}C_{12}$N][Br]** and **[C_1C_{12}Im][Br]**) and with the one of **[Ch][Cl]**, to dissect the cation and anion contribution. For the sake of comparison, cytotoxicity of folic acid was also investigated. The IC_{50} values (Table 6) were calculated from a dose-response model, by fitting sigmoidal curves of the cell percentage inhibition *versus* the logarithmic of salts concentration (Figure S15).

Table 6. Concentration of salts (IC_{50} expressed in μM) at which the proliferation of breast cancer MDA-MB-231 and MCF-7 and the normal hTERT RPE-1 cells was inhibited by 50% with respect to the untreated growth control, after 24 h of treatment.

IC50 μM ± SD

	MDA-MB-231	**MCF-7**	**hTERT RPE-1**
Folic Acid (FA)	> 100	> 100	> 100
$[C_{222}C_{12}N]_2$[Folate]	2.33 ± 0.31	2.78 ± 0.35	9.55 ± 0.81
$[Ch]_2$[Folate]	> 100	> 100	> 100
$[C_1C_{12}Im]_2$[Folate]	2.01 ± 0.28	3.30 ± 0.35	12.22 ± 1.12
$[C_{222}C_{12}N]$[Br]	5.36 ± 0.6	4.35 ± 0.42	17.11 ± 1.5
[Ch][Cl]	> 100	> 100	> 100
$[C_1C_{12}Im]$[Br]	4.47 ± 0.5	3.07 ± 0.32	18.16 ± 2.1

No significant effect on viability was observed in cells treated with FA compared with the control cells at least up to 100 μM, corresponding to the maximum concentration tested. Conversely, a more articulate behavior was detected when salts were used and different trends were obtained as a function of the cation or anion structure (Figure 9).

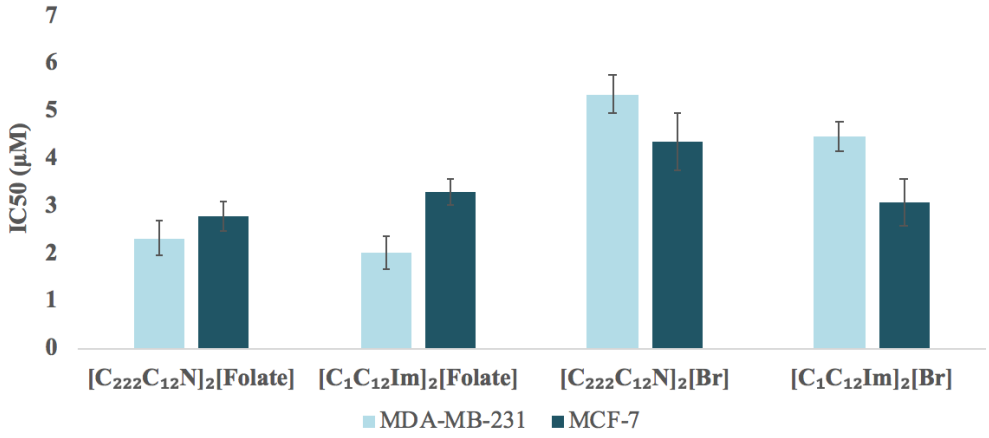

Figure 9. IC_{50} values expressed as μM concentration of **$[C_{222}C_{12}N]_2$[Folate]**, **$[C_1C_{12}Im]_2$[Folate]**, **[$C_{222}C_{12}$N][Br]** and **[C_1C_{12}Im][Br]** toward MDA-MB-231 and MCF-7 breast cancer cell lines after 24 h of treatments. The data are expressed as mean value ± SD.

Among tested salts, cholinium-based ones did not exert cytotoxic effects on both breast cancer cell lines, exhibiting IC_{50} > 100 μM, perfectly recalling the low cytotoxicity of cholinium-based ionic liquids against different cell lines, previously reported in literature.[73-75] Differently, the presence of a long alkyl chain on both ammonium and imidazolium cations induced significant cytotoxic effects, with IC_{50} ranging from 2.01±0.28 μM for **$[C_1C_{12}Im]_2$[Folate]** to 5.36±0.6 μM for **[$C_{222}C_{12}$N][Br]** in MDA-MB-231 cells. Analytically, the effect of the cation ([$C_1C_{12}Im^+$] *versus* [$C_{222}C_{12}N^+$]) on cell viability was more evident when the bromide salts were taken into consideration. Indeed, in the case of [Folate]-based salts, the cell line being the same, IC_{50} values were comparable independently from the cation structure. Differently, in the case of bromide salts, IC_{50} values gradually increased on going from [$C_1C_{12}Im^+$] to [$C_{222}C_{12}N^+$], accounting for a higher cytotoxicity of imidazolium salt with respect the corresponding ammonium one (Figure 9). Cytotoxicity of halide-based ionic liquids and organic salts, bearing long alkyl chain on the cation

structure, is well documented in literature.[16, 76, 77] Furthermore, our results perfectly agree with previous reports claiming the higher cytotoxicity of aromatic imidazolium based salts with respect to the corresponding ammonium ones.[78]

To rationalize the above results, we took in consideration differences in the anion nature and in their "recognition" by cell lines. Bromide and folate anion firstly differ for their hydrophobicity. In particular, the highly lipophilic skeleton of folate surely awards corresponding salts of a higher ability to interact and cross cell membranes than the corresponding bromide ones. On the other hand, as previously stated, MDA-MD-231 cell line expresses high level of folate receptor, that probably further favors the uptake of the corresponding salts through a receptor mediated internalization. Taking in consideration results obtained by UV-vis and fluorescence investigation in the presence of BSA and in the light of the above hypotheses, it is reasonable to expect different uptake rates as a function of the anion nature. This should be higher in the case of folate than in the case of bromide salts. Consequently, cell line being the same, in the case of [Folate]-based salts, a fast salt uptake probably occurred that does not allow to distinguish differences in the cation structure and gave rise to the obtainment of comparable IC_{50} values for imidazolium and ammonium salts. In few words, the fast uptake caused low selectivity in the structure recognition. Differently, in the case of bromide salts, a slower salt uptake better allowed discriminating the different nature of the cationic head, bringing to significantly different cytotoxicity. On this subject, a relevant example about the relationship operating between the rate of uptake and cytotoxic effects has been previously reported by Gray *et al*, studying antiproliferative activity of some derivatives of gallium(III) tris(pentafluorophenyl)corrole.[79] The above hypothesis is also supported by the differences in IC_{50} detected for folate salts in the case of MCF-7, that overexpress only low levels of receptor.

Comparing results obtained as a function of cell line nature, in the presence of folate salts, demonstrates comparable IC_{50} values were collected for **$[C_{222}C_{12}N]_2$[Folate]**. Differently, for **$[C_1C_{12}Im]_2$[Folate]**, IC_{50} increases going from MDA-MB-231 to MCF-7, according to the better salt uptake occurring in the first case.

As for bromide salts, a more homogeneous behavior was detected. Indeed, independently from the cation structure, IC_{50} values decreased going from MDA-MB-231 to MCF-7.

A further support to the above hypothesis comes also from the significant morphological changes observed in a dose and time-dependent manner, both in MDA-MB-231 and MCF-7 cells treated cells (Figure 10 and S16). Indeed, the MDA-MB-231 cells were more sensitive to cellular damage, at least in the first hours of treatments, once again suggesting that folate salts could be internalized faster in MDA-MB-231 than MCF-7. Both MDA-MB-231 and MCF-7 treated cells showed long cell projections (black arrows), whose length increases with the salt concentration. MCF-7 treated cells appear vacuolated and also in this case number and size of modified cells increase with salt concentration. Based on the morphology abnormalities and IC_{50} values, we surmise that additional mechanisms could work to determine the cytotoxic effects, such as the ability of salts to cross biological membranes, triggering cell death mechanisms. Accordingly, no osmotic effects or significant cellular swellings or wrinkling were recorded. The molecular nature and the functional significance of the cell projections and vacuoles deserve further investigations.

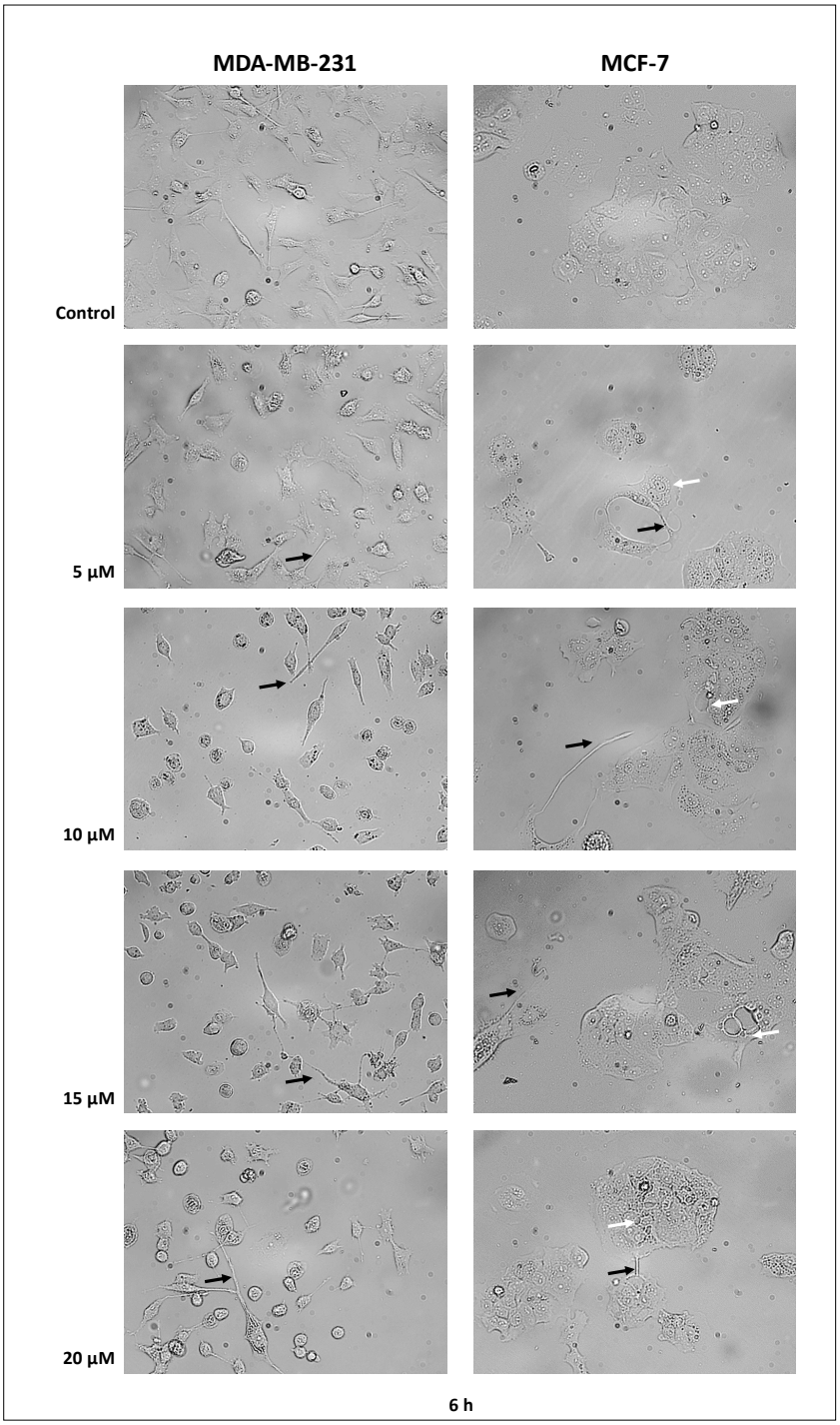

Figure 10. Inverted-phase contrast micrographs of MDA-MB-231 and MCF-7 cells treated for 6h with increasing concentrations (5-10-15-20 µM) of **$[C_1C_{12}Im]_2$[Folate]**. Magnification 200X.

Selectivity towards cancer cells. To verify the cancer selectivity index (CSI), defined as the ratio of IC_{50} of normal hTERT RPE-1 to that of breast cancer MDA-MB-231 and MCF-7 cells, cytotoxicity was also evaluated on the non-tumoral epithelial cell line hTERT RPE-1 (Figure 11). Results show selective cytotoxicity of all investigated salts towards the cancer cell lines compared to normal cells (CSI > 3). The **$[C_1C_{12}Im]_2$[Folate]** showed the most relevant selectivity; it was more cytotoxic against the MDA-MB-231 (IC_{50} 2.01 ± 0.28 μM) than the hTERT RPE-1 cells (IC_{50} 12.22 ± 1.12 μM), displaying a selectivity index of 6.08 ± 0.6, suggesting a more selective targeting of **$[C_1C_{12}Im]_2$[Folate]** in cancer cells overexpressing the FRs. In the case of both folate and bromide salts, the highest selectivity index was obtained for imidazolium salts. Interestingly, the trend in selectivity index also changes as a function of anion nature. Indeed, in the case of folate salts, it was higher for MDA-MB-231. Conversely, in the case of bromide salts, higher CSI values were detected for MCF-7 with respect to MDA-MD-231. In both cases, differences as a function of cell line nature were also more significant with respect to the ones observed for ammonium salts.

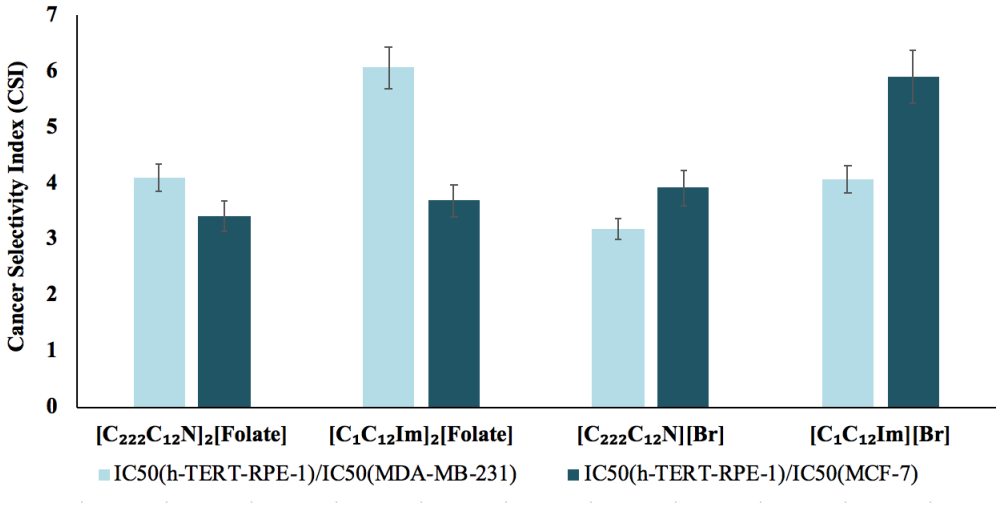

Figure 11. Cancer Selectivity Index (CSI) defined as ratio of IC_{50} values after 24 h of treatments of normal epithelial cells hTERT RPE-1 and MDA-MB-231 and MCF-7 breast cancer cells lines, respectively for **$[C_{222}C_{12}N]_2$[Folate]**, **$[C_1C_{12}Im]_2$[Folate]**, **$[C_{222}C_{12}N]$[Br] and $[C_1C_{12}Im]_2$[Br]**. The data are expressed as mean value ± SD.

Uptake of Folate salts. To prove the selective uptake of folate salts inside MDA-MB-231 cells through the folate receptor, the MTT assay was performed by treating the cells with folic acid-free medium (Figure 12). As expected, a significant decrease of IC_{50} values was recorded for MDA-MB-231 cells, especially for **$[C_1C_{12}Im]_2$[Folate]**, once again accounting for the higher cytotoxicity of imidazolium salts with respect to the corresponding ammonium one. On the other hand, a negligible decrease was observed in MCF-7 cells, confirming the more selective targeting of folate salts in folate receptor overexpressing cells.

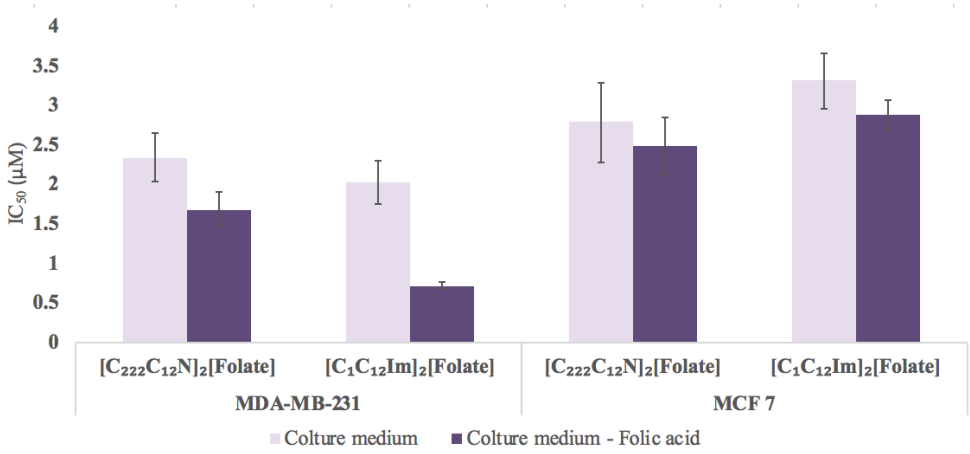

Figure 12. IC_{50} values expressed as µM concentration of **$[C_{222}C_{12}N]_2$[Folate]** and **$[C_1C_{12}Im]_2$[Folate]** toward MDA-MB-231 and MCF-7 breast cancer cell lines after 24 h of treatments in complete culture medium and Acid Folic-free culture medium. The data are expressed as mean value ± SD.

Effect of folate salts treatment on intracellular oxygen species. Oxidative stress, which is characterized by excessive production of reactive oxygen species (ROS), is a common pathway inducing cell death. ROS interacting with intracellular biological macromolecules, including nuclear acids, proteins, and lipids, may induce disfunction of mitochondria and activate several apoptotic signaling pathways. To verify if cytotoxicity depends on the induction of oxidative stress, which in turn induces cell death through several supposed molecular mechanisms, ROS generation was determined by dichlorodihydrofluorescein diacetate (DCFH-DA). As shown in Figure 13, after 24 h of treatment, both **$[C_1C_{12}Im]_2$[Folate]** and **$[C_{222}C_{12}N]_2$[Folate]** induced a remarkable ROS increase in a concentration-dependent manner, with a minimum of 2 fold increase for the lowest concentration (0.2 μM) and a maximum of about 4 fold increase for the highest concentration of treatment (3.6 μM) in both cell lines, irrespective of the nature of the cation,

suggesting a central role of ROS in cell death induction, regardless of the uptake mechanism (receptor-mediated endocytosis or direct crossing of biological membranes).

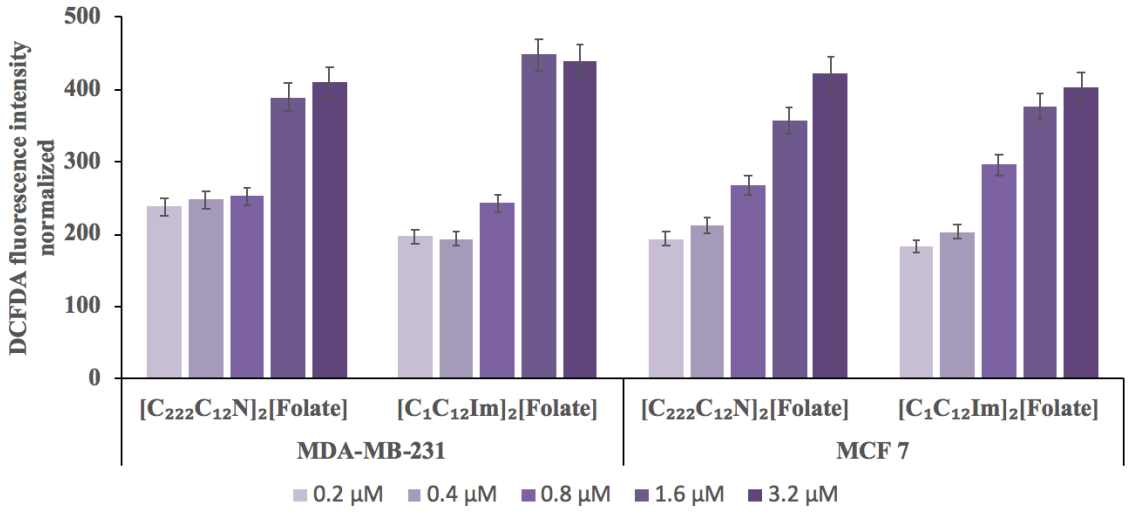

Figure 13. ROS were measured in MDA-MB-231 and MCF-7 cells after 24 h of treatment with increasing concentrations (0.2, 0.4, 0.8, 1.6 and 3.2 µM) of **$[C_1C_{12}Im]_2[Folate]$** and **$[C_{222}C_{12}N]_2[Folate]$** using DCFH-DA and quantified through spectrofluorometry. Data were normalized for cell number determined by MTT assay and expressed as percentage in respect to the untreated cells used as control. The data are expressed as mean value ± SD.

Biological activity of gel phases. To verify if organic salts retained their biological activity also in gel phase, the soft material formed by **$[C_1C_{12}Im]_2[Folate]$** in TBS/DMSO, at 6 wt %, was used as model system. This was chosen for its ability to keep its gel nature during the contact with culture medium. Obviously, in this case antiproliferative activity could be only related to the release of

the gelator from the gelatinous network. The gel phase was formed on a coverslip and in the first set of experiments, it was added to the breast cancer cells (MDA-MB-231 and MCF-7), seeded in 6-well plates. This was aimed to verify if the release of the gelator from the gel could prevent adhesion and therefore cell growth (Figure 14a). Interestingly, treated cells failed to adhere and after 24 hours of incubation no cells survived the treatment, suggesting that the gelator was released from gel at toxic concentrations, higher than IC_{50}. Subsequently, the coverslip containing the gel was moved into new cell plates containing the breast cancer cells (MDA-MB-231 and MCF-7) seeded 24h before. After 3h of incubation, the gel was hydrated and several fragments were found inside the well, while both breast cancer cells lost their morphology and were already dead (Figure 14b), suggesting that even after 24h of release the gel continues to release toxic concentrations.

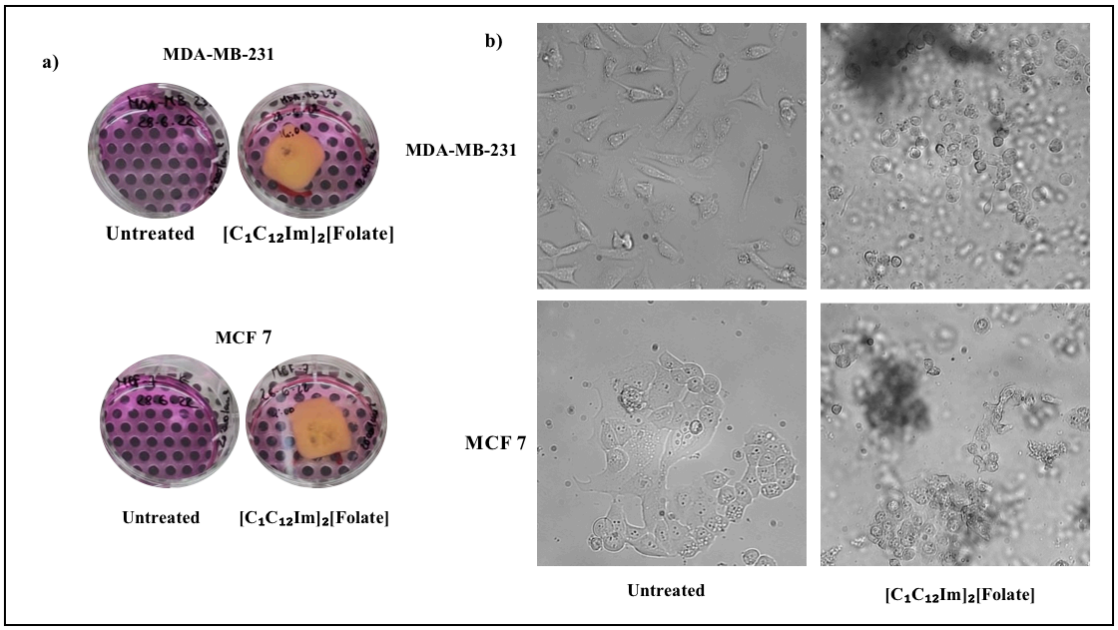

Figure 14. Morphological changes induced by **$[C_1C_{12}Im]_2$[Folate]** gel in MDA-MB-231 and MCF-7 cells after 3 h of treatment. **a)** Micrographs of cell plates control and treated with **$[C_1C_{12}Im]_2$[Folate]** and **b)**

Inverted-phase contrast micrographs of MDA-MB-231 and MCF-7 cells treated for 3h with **$[C_1C_{12}Im]_2$[Folate]** gel. Magnification 200X.

A second set of experiments was carried out by dipping the coverslip containing the **$[C_1C_{12}Im]_2$[Folate]** gel inside a Petri dish containing 20 mL of culture medium. A total of 1 mL of medium was picked up every 24h for 96h, for a total of 4 withdrawals. Each sample was appropriately diluted (from 1 to 16 to 1 to 256) and used to treat both MDA-MB-231 and MCF-7 cells, seeded 24h before the treatment (Figure 15a), and cell morphology monitored after 1h, 4h, and 24h. Interestingly, the cytotoxic effect was dose and time dependent. In particular, already after 1h of incubation the samples diluted 1 to 32 showed a different toxic effect toward the breast cancer cell lines, being more toxic with MDA-MB-231 than MCF-7 (Figure 15b, c). Since the same trend is maintained over the time (4h and 24h), this suggests that the cytotoxic mechanism for **$[C_1C_{12}Im]_2$[Folate]** does not change as a consequence of the salt entrapment in the gel phase, exhibiting also in this case a selective uptake towards MBA-MD-231 cells, overexpressing folate receptor.

a)

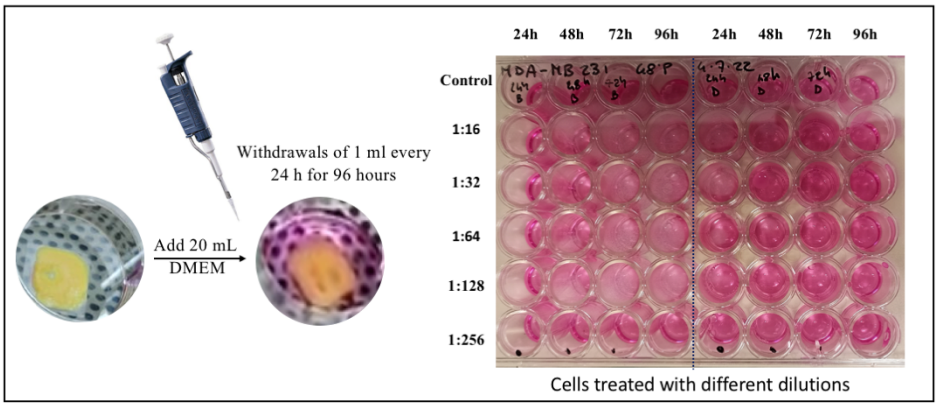
Withdrawals of 1 ml every
24 h for 96 hours
Add 20 mL
DMEM
24h 48h 72h 96h 24h 48h 72h 96h
Control
1:16
1:32
1:64
1:128
1:256
Cells treated with different dilutions

b)

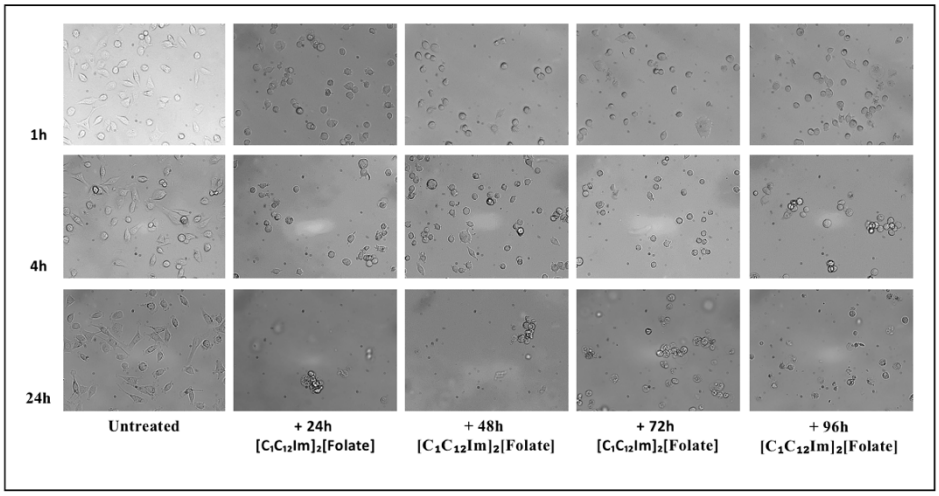
MDA-MB-231
1h
4h
24h
Untreated
+ 24h [C1C12Im]2[Folate]
+ 48h [C1C12Im]2[Folate]
+ 72h [C1C12Im]2[Folate]
+ 96h [C1C12Im]2[Folate]

c)

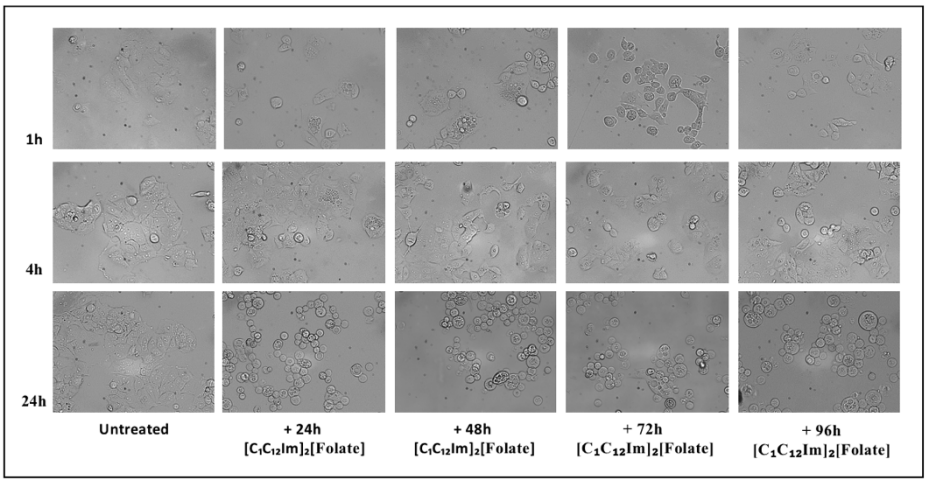
MCF-7
1h
4h
24h
Untreated
+ 24h [C1C12Im]2[Folate]
+ 48h [C1C12Im]2[Folate]
+ 72h [C1C12Im]2[Folate]
+ 96h [C1C12Im]2[Folate]

Figure 15. Biological activity of gelator released from **[$C_1C_{12}Im]_2$[Folate]-**derived gel in MDA-MB-231 and MCF-7 cells. **a)** The **[$C_1C_{12}Im]_2$[Folate]** gel, prepared on a coverslip and added into a Petri dish containing 20 mL of culture medium; **b)** Micrographs of MDA-MB-231 and **c)** MCF-7 cells incubated for 1h, 4 h and 24 h with the gelator released (diluted 1 to 32), from **[$C_1C_{12}Im]_2$[Folate]** gel, picked up after 24h, 48h, 72 h and 96 h. Magnification 200X.

Conclusions

Chemotherapeutic targeted agents were obtained combining the properties of ammonium and imidazolium cations with the ones of folate anions. Folate-based organic salts were firstly investigated for their photophysical behavior. In particular, self-assembly ability was analyzed in buffer solutions and their binary mixtures with DMSO. They proved able to form supramolecular fluorescent aggregates, not only in solution but also in the solid state. In the case of **[$C_1C_{12}Im]_2$[Folate]**, spectroscopic evidence gave insights about the formation of *J*-aggregates. The propensity to self-assembly also awarded the above salt gelation ability.

Properties of supramolecular gels were significantly affected by the nature of the gelled solvent (buffer solution or buffer/DMSO binary mixture). Interestingly, it was possible to identify a precise relationship among gel-sol transition temperature, mechanical properties and morphology of a given gel phase.

With the aim to investigate possible biological activity, folate based organic salts were tested towards two cancer cell lines, namely MDA-MB-231 and MCF-7, overexpressing high and low levels of folate receptor. Results of cell viability tests demonstrated that cellular uptake occur at different rate, in dependence of the level of folate receptor overexpression. This in turn affects the

mechanism of interaction that can occur by simple membrane crossing (MCF-7), driven by salt hydrophobicity, or a more articulate receptor-mediated internalization also supported by membrane crossing (MDA-MB-231). As a consequence, selectivity in terms of both salts structure and cancer cell line nature was observed. Interestingly, higher cancer selectivity indexes were obtained towards cancer cell line over normal epithelial cells for both **[C_1C_{12}Im]$_2$[Folate]** and **[C_1C_{12}Im][Br]**. However, the salts selectively act towards different cancer cell lines, namely MDA-MB-231, in the case of **[C_1C_{12}Im]$_2$[Folate]**, and MCF-7 in the case of **[C_1C_{12}Im][Br]**. This depends on the ability of the cell line to overexpress or not folate receptor.

Results obtained from DCFH-DA test allowed demonstrating that, independently from cancer cell line and cation nature, in the case of folate-based organic salts, cell death could be induced by oxidative stress.

Cytotoxic effects of organic salts were also retained in gel phase with no significant changes in the uptake mechanism.

Associated Content

Electronic Supplementary Information. UV-vis and fluorescence spectra for organic salts in buffer and buffer/DMSO solutions, DLS investigation in buffer and buffer/DMSO solutions, fluorescence spectra for determination of emission quantum yield, fluorescence spectra of organic salts in solid phase, ATR-FTIR spectra for organic salts and gel phases, plots of strain and frequency sweep measurements on gel phases, RLS spectra of organic salts in solution, emission spectra for hot solutions and corresponding gel phases, cytotoxicity curves of salts, Inverted-phase

contrast micrographs of cell lines after treatment with the salts solutions, ^{1}H and ^{13}C NMR spectra of salts, table of gelation tests, table for RLS intensity for gel phases. This material is available free of charge.

Author Information

Corresponding Author

Francesca D'Anna, Università degli Studi di Palermo, Dipartimento STEBICEF, Viale delle Scienze, Ed. 17, 90128 Palermo (Italy). E-mail: francesca.danna@unipa.it

Author Contributions

The manuscript was written through contributions of all authors. All authors have given approval to the final version of the manuscript.

Acknowledgment

We thank the University of Palermo for financial support (FFR 2021). C.R. thanks PNR, Next Generation EU, DM737/2021, CUP B79J21038330001.

References

1. H. Sung, J. Ferlay, R. L. Siegel, M. Laversanne, I. Soerjomataram, A. Jemal and F. Bray, *CA: A Cancer Journal for Clinicians*, 2021, **71**, 209-249.
2. K.-H. Altmann, *Chimia*, 2018, **72**, 154.
3. N. Krall, F. Pretto, W. Decurtins, G. J. L. Bernardes, C. T. Supuran and D. Neri, *Angew. Chem., Int. Ed.*, 2014, **53**, 4231-4235.
4. M. Srinivasarao, C. V. Galliford and P. S. Low, *Nat. Rev. Drug Discovery*, 2015, **14**, 203-219.

5. R. van der Meel, L. J. C. Vehmeijer, R. J. Kok, G. Storm and E. V. B. van Gaal, in *Intracellular Delivery III: Market Entry Barriers of Nanomedicines*, eds. A. Prokop and V. Weissig, Springer International Publishing, Cham, 2016, DOI: 10.1007/978-3-319-43525-1_7, pp. 163-200.
6. X.-X. Zhang, H. S. Eden and X. Chen, *J. Controlled Release*, 2012, **159**, 2-13.
7. W. Xia and P. S. Low, *J. Med. Chem.*, 2010, **53**, 6811-6824.
8. P. S. Low, W. A. Henne and D. D. Doorneweerd, *Acc. Chem. Res.*, 2008, **41**, 120-129.
9. M. D. A. Salazar and M. Ratnam, *Cancer Metastasis Rev.*, 2007, **26**, 141-152.
10. S. D. Weitman, A. G. Weinberg, L. R. Coney, V. R. Zurawski, D. S. Jennings and B. A. Kamen, *Cancer Res.*, 1992, **52**, 6708-6711.
11. R. Zhao, S. H. Min, Y. Wang, E. Campanella, P. S. Low and I. D. Goldman, *J. Biol. Chem.* , 2009, **284**, 7.
12. S. Kim, J.-H. Kim, O. Jeon, I. C. Kwon and K. Park, *Eur. J. Pharm. Biopharm.*, 2009, **71**, 420-430.
13. J. F. Ross, P. K. Chaudhuri and M. Ratnam, *Cancer*, 1994, **73**, 2432-2443.
14. N. Nakashima-Matsushita, T. Homma, S. Yu, T. Matsuda, N. Sunahara, T. Nakamura, M. Tsukano, M. Ratnam and T. Matsuyama, *Arthritis Rheumatol.*, 1999, **42**, 1609-1616.
15. A. L. Jackman, D. S. Theti and D. D. Gibbs, *Adv. Drug Delivery Rev.*, 2004, **56**, 1111-1125.
16. P. Cancemi, M. Buttacavoli, F. D'Anna, S. Feo, R. M. Fontana, R. Noto, A. Sutera, P. Vitale and G. Gallo, *New J. Chem.*, 2017, **41**, 3574-3585.
17. C. Rizzo, P. Cancemi, L. Mattiello, S. Marullo and F. D'Anna, *ACS Appl. Mater. Interfaces*, 2020, **12**, 48442-48457.
18. S. Bonazzi, M. M. DeMorais, G. Gottarelli, P. Mariani and G. P. Spada, *Angew. Chem., Int. Ed.*, 1993, **32**, 248-250.
19. F. Ciuchi, G. Di Nicola, H. Franz, G. Gottarelli, P. Mariani, M. G. Ponzi Bossi and G. P. Spada, *J. Am. Chem. Soc.*, 1994, **116**, 7064-7071.
20. F. Billeci, F. D'Anna, S. Marullo and R. Noto, *RSC Adv.*, 2016, **6**, 59502-59512.
21. F. D'Anna, S. Marullo, G. Lazzara, P. Vitale and R. Noto, *Chem. Eur. J.*, 2015, **21**, 14780-14790.
22. F. D'Anna, C. Rizzo, P. Vitale, G. Lazzara and R. Noto, *Soft Matter*, 2014, **10**, 9281-9292.
23. F. Billeci, F. D'Anna, H. Q. N. Gunaratne, N. V. Plechkova and K. R. Seddon, *Green Chem.*, 2018, **20**, 4260-4276.
24. C. Rizzo, R. Arrigo, N. T. Dintcheva, G. Gallo, F. Giannici, R. Noto, A. Sutera, P. Vitale and F. D'Anna, *Chem. Eur. J.*, 2017, **23**, 16297-16311.
25. A. R. Hirst, B. Escuder, J. F. Miravet and D. K. Smith, *Angew. Chem., Int. Ed.*, 2008, **47**, 8002-8018.
26. N. M. Sangeetha and U. Maitra, *Chem. Soc. Rev.*, 2005, **34**, 821-836.
27. C. Mortier, D. C. S. Costa, M. B. Oliveira, H. J. Haugen, S. P. Lyngstadaas, J. J. Blaker and J. F. Mano, *Mater. Today Chem.*, 2022, **26**, 101222.
28. J. Karvinen and M. Kellomäki, *Eur. Polym. J.*, 2022, **181**, 111641.
29. N. Aktas, D. Alpaslan and T. E. Dudu, *Frontiers in Materials*, 2022, **9**.
30. P. Moharana and G. Santosh, *J. Phys. Org. Chem.*, 2022, **35**, e4408.
31. G. Zhao, B. Lv, H. Wang, B. Yang, Z. Li, R. Junfang, G. Gui, W. Liu, S. Yang and L. Li, *Int. J. Smart Nano Mater.*, 2021, **12**, 307-336.

32. W. P. Singh, U. Koch and R. S. Singh, *Soft Materials*, 2020, **18**, 386-410.
33. Q. Cheng, A. Hao and P. Xing, *ACS Nano*, 2022, **16**, 6825-6834.
34. H. Sun, B. Zhang, L. Lu, Z. Chen, Y. Huo, W. Li, B. Zhang and J. Song, *Chem. Eng. J. (Lausanne)*, 2023, **451**, 139051.
35. J. Bachl, S. Oehm, J. Mayr, C. Cativiela, J. J. Marrero-Tellado and D. Díaz Díaz, *Int. J. Mol. Sci.*, 2015, **16**, 11766-11784.
36. C. Rizzo, A. Mandoli, S. Marullo and F. D'Anna, *J. Org. Chem.*, 2019, **84**, 6356-6365.
37. L. Yan, G. Li, Z. Ye, F. Tian and S. Zhang, *Chem. Commun.*, 2014, **50**, 14839-14842.
38. F. D'Anna, F. Ferrante and R. Noto, *Chemistry – A European Journal*, 2009, **15**, 13059-13068.
39. D. J. Abdallah and R. G. Weiss, *Langmuir*, 2000, **16**, 352-355.
40. S. R. Raghavan and B. H. Cipriano, in *Molecular Gels: Materials with Self-Assembled Fibrillar Networks*, eds. R. G. Weiss and P. Terech, Springer Netherlands, Dordrecht, 2006, DOI: 10.1007/1-4020-3689-2_9, pp. 241-252.
41. R. Musso, G. Di Cara, N. N. Albanese, M. R. Marabeti, P. Cancemi, D. Martini, E. Orsini, C. Giordano and I. Pucci-Minafra, *J. Proteomics*, 2013, **90**, 115-125.
42. I. Pucci-Minafra, N. N. Albanese, G. Di Cara, L. Minafra, M. R. Marabeti and P. Cancemi, *Connect. Tissue Res.*, 2008, **49**, 252-256.
43. M. L. Saladino, M. Markowska, C. Carmone, P. Cancemi, R. Alduina, A. Presentato, R. Scaffaro, D. Biały, M. Hasiak, D. Hreniak and M. Wawrzyńska, *Materials*, 2020, **13**, 1980.
44. M. V. Raimondi, A. Presentato, G. Li Petri, M. Buttacavoli, A. Ribaudo, V. De Caro, R. Alduina and P. Cancemi, *Antibiotics*, 2020, **9**, 292.
45. Z. Wu, A. Shah, N. Patel and X. Yuan, *Bioorg. Med. Chem. Lett.*, 2010, **20**, 5108-5112.
46. L. K. Li, A.-S. Rola, F. A. Kaid, A. M. Ali and A. M. Alabsi, *Arch. Oral Biol.*, 2016, **64**, 28-38.
47. Y. Kamikawa, M. Nishii and T. Kato, *Chem. Eur. J.*, 2004, **10**, 5942-5951.
48. P. Xing, X. Chu, M. Ma, S. Li and A. Hao, *Phys. Chem. Chem. Phys.*, 2014, **16**, 8346-8359.
49. C.-T. Chen, C.-H. Chen and T.-G. Ong, *J. Am. Chem. Soc.*, 2013, **135**, 5294-5297.
50. T. F. A. De Greef, M. M. J. Smulders, M. Wolffs, A. P. H. J. Schenning, R. P. Sijbesma and E. W. Meijer, *Chem. Rev. (Washington, DC, U. S.)*, 2009, **109**, 5687-5754.
51. E. E. Jelley, *Nature*, 1936, **138**, 1009-1010.
52. C. Hao, J. Gao, Y. Wu, X. Wang, R. Zhao, S. Mei, J. Yang, X. Zhai and H. Qiu, *React. Funct. Pol.*, 2018, **122**, 140-147.
53. W. Liang, Z. Zhang, Q. Zhu, Z. Han, C. Huang, X. Liang and M. Yang, *Spectrochim. Acta, Part A*, 2023, **287**, 122054.
54. M. T. A. Qashqoosh, Y. K. Manea, F. A. M. Alahdal and S. Naqvi, *BioNanoScience*, 2019, **9**, 848-858.
55. L. P. Jameson, N. W. Smith, O. Annunziata and S. V. Dzyuba, *Phys. Chem. Chem. Phys.*, 2016, **18**, 14182-14185.
56. A. Ajayaghosh and V. K. Praveen, *Acc. Chem. Res.*, 2007, **40**, 644-656.
57. F. Würthner, T. E. Kaiser and C. R. Saha-Möller, *Angew. Chem., Int. Ed.*, 2011, **50**, 3376-3410.
58. Lakowicz and J. R., *Solvent, Environmental Effects. In Principles of fluorescence spectroscopy*, 2006.
59. S. Fery-Forgues and D. Lavabre, *J. Chem. Educ.*, 1999, **76**, 1260.

60. J. He, B. Xu, F. Chen, H. Xia, K. Li, L. Ye and W. Tian, *J. Phys. Chem. C*, 2009, **113**, 9892-9899.
61. D. O. Scanlon, A. Walsh and G. W. Watson, *Chem. Mater.*, 2009, **21**, 4568-4576.
62. Q. Wu, T. Zhang, Q. Peng, D. Wang and Z. Shuai, *Phys. Chem. Chem. Phys.*, 2014, **16**, 5545-5552.
63. W. Z. Yuan, Y. Tan, Y. Gong, P. Lu, J. W. Y. Lam, X. Y. Shen, C. Feng, H. H.-Y. Sung, Y. Lu, I. D. Williams, J. Z. Sun, Y. Zhang and B. Z. Tang, *Adv. Mater.*, 2013, **25**, 2837-2843.
64. S. Raghavan and B. Cipriano, *Gel Formation: Phase Diagrams Using Tabletop Rheology and Calorimetry*, Springer Dordrecht, 2006.
65. Y. Song, J. Gao, X. Xu, H. Zhao, R. Xue, J. Zhou, W. Hong and H. Qiu, *Mater. Sci. Eng. C*, 2017, **75**, 706-713.
66. J. Anglister and I. Z. Steinberg, *J. Chem. Phys.*, 1983, **78**, 5358-5368.
67. C. Rizzo, R. Arrigo, N. T. Dintcheva, G. Gallo, F. Giannici, R. Noto, A. Sutera, P. Vitale and F. D'Anna, *Chemistry – A European Journal*, 2017, **23**, 16297-16311.
68. R. F. Pasternack and P. J. Collings, *Science*, 1995, **269**, 935-939.
69. R. Meier, T. D. Henning, S. Boddington, S. Tavri, S. Arora, G. Piontek, M. Rudelius, C. Corot and H. E. Daldrup-Link, *Radiology*, 2010, **255**, 527-535.
70. T. Yang, F. Xu, D. Fang and Y. Chen, *Scientific Reports*, 2015, **5**, 16733.
71. A. Angelopoulou, A. Kolokithas-Ntoukas, C. Fytas and K. Avgoustakis, *ACS Omega*, 2019, **4**, 22214-22227.
72. J. P. Marshalek, P. S. Sheeran, P. Ingram, P. A. Dayton, R. S. Witte and T. O. Matsunaga, *J Control Release*, 2016, **243**, 69-77.
73. T. E. Sintra, A. Luís, S. N. Rocha, A. I. M. C. Lobo Ferreira, F. Gonçalves, L. M. N. B. F. Santos, B. M. Neves, M. G. Freire, S. P. M. Ventura and J. A. P. Coutinho, *ACS Sustain. Chem. Eng.*, 2015, **3**, 2558-2565.
74. X. Wang, C. A. Ohlin, Q. Lu, Z. Fei, J. Hu and P. J. Dyson, *Green Chem.*, 2007, **9**, 1191-1197.
75. M. Demurtas, V. Onnis, P. Zucca, A. Rescigno, J. I. Lachowicz, L. De Villiers Engelbrecht, M. Nieddu, G. Ennas, A. Scano, F. Mocci and F. Cesare Marincola, *ACS Sustain. Chem. Eng.*, 2021, **9**, 2975-2986.
76. C. Rizzo, P. Cancemi, L. Mattiello, S. Marullo and F. D'Anna, *ACS Appl. Mater. Interfaces*, 2020, **12**, 48442-48457.
77. J. Arning and M. Matzke, *Curr. Org. Chem.*, 2011, **15**, 1905-1917.
78. K. S. Egorova and V. P. Ananikov, *ChemSusChem*, 2014, **7**, 336-360.
79. M. Pribisko, J. Palmer, R. H. Grubbs, H. B. Gray, J. Termini and P. Lim, *PNAS*, 2016, **113**, E2258-E2266.

Table of Contents Entry